



HAL
open science

Induced Seismicity Controlled by Injected Hydraulic Energy: The Case Study of the EGS Soutz-Sous-Forêts Site

K. Drif, O. Lengliné, J. Kinscher, J. Schmitbuhl

► **To cite this version:**

K. Drif, O. Lengliné, J. Kinscher, J. Schmitbuhl. Induced Seismicity Controlled by Injected Hydraulic Energy: The Case Study of the EGS Soutz-Sous-Forêts Site. *Journal of Geophysical Research : Solid Earth*, 2024, 129 (6), 10.1029/2023JB028190 . ineris-04614270

HAL Id: ineris-04614270

<https://ineris.hal.science/ineris-04614270>

Submitted on 17 Jun 2024

HAL is a multi-disciplinary open access archive for the deposit and dissemination of scientific research documents, whether they are published or not. The documents may come from teaching and research institutions in France or abroad, or from public or private research centers.

L'archive ouverte pluridisciplinaire **HAL**, est destinée au dépôt et à la diffusion de documents scientifiques de niveau recherche, publiés ou non, émanant des établissements d'enseignement et de recherche français ou étrangers, des laboratoires publics ou privés.



Distributed under a Creative Commons Attribution - NonCommercial 4.0 International License

JGR Solid Earth

RESEARCH ARTICLE

10.1029/2023JB028190

Induced Seismicity Controlled by Injected Hydraulic Energy: The Case Study of the EGS Soultz-Sous-Forêts Site

K. Drif^{1,2} , O. Lengliné¹ , J. Kinscher² , and J. Schmitbuhl¹ 

¹Université de Strasbourg/CNRS, EOST/ITES, Strasbourg, France, ²Institut national de l'environnement industriel et des risques (INERIS), Nancy, France

Key Points:

- Homogenization over multiple stimulations at the Soultz-sous-Forêts enhanced geothermal system site of the seismic moment estimates of the induced seismicity
- The ratio of the radiated seismic energy and the hydraulic energy is shown to be constant during stimulations
- This ratio can be seen as a reservoir property describing its seismic response to fluid injection and is used to predict the largest magnitude of induced earthquakes

Supporting Information:

Supporting Information may be found in the online version of this article.

Correspondence to:

K. Drif,
kamel.drif@ineris.fr

Citation:

Drif, K., Lengliné, O., Kinscher, J., & Schmitbuhl, J. (2024). Induced seismicity controlled by injected hydraulic energy: The case study of the EGS Soultz-sous-Forêts site. *Journal of Geophysical Research: Solid Earth*, 129, e2023JB028190. <https://doi.org/10.1029/2023JB028190>

Received 2 NOV 2023

Accepted 14 MAY 2024

Author Contributions:

Conceptualization: K. Drif, O. Lengliné, J. Kinscher, J. Schmitbuhl

Formal analysis: K. Drif, O. Lengliné

Funding acquisition: J. Kinscher, J. Schmitbuhl

Investigation: K. Drif, J. Schmitbuhl

Methodology: K. Drif, O. Lengliné

Project administration: O. Lengliné, J. Kinscher, J. Schmitbuhl

Software: K. Drif

Supervision: O. Lengliné, J. Kinscher, J. Schmitbuhl

Validation: K. Drif, O. Lengliné

Visualization: K. Drif

© 2024 The Authors.

This is an open access article under the terms of the [Creative Commons Attribution-NonCommercial License](https://creativecommons.org/licenses/by/4.0/), which permits use, distribution and reproduction in any medium, provided the original work is properly cited and is not used for commercial purposes.

Abstract How induced seismicity in deep geothermal project (enhanced geothermal systems, EGS) is controlled by fluid injection is of central importance for monitoring the related seismic risk. Here we analyze the relationship between the radiated seismic energy and the hydraulic energy related to the fluid injection during several hydraulic stimulations and circulation tests at Soultz-sous-Forêts geothermal site. Based on a harmonized database, we show that the ratio between these energies is at first order constant during stimulations and of the same magnitude independently of the stimulation protocol and injection depth. Re-stimulations are characterized by a sharp evolution of this ratio during injection which ultimately converges to the characteristic value of the reservoir. This supports that the seismicity is caused by the relaxation of the pre-existing strain energy in the stimulated volume, rather than by the deformation generated from fluid injection. The ratio appears as an intrinsic large-scale property of the reservoir that can be assessed at the very beginning of the first stimulation. Based on this property, we suggest a way to predict the largest magnitude of the induced seismic events knowing the maximum targeted hydraulic energy of the injection.

Plain Language Summary Monitoring and predicting fluid-injection-induced seismicity is a major concern for the development of the geothermal energy. Several geothermal sites have shown a linear relationship between the radiated seismic energy and the hydraulic energy, suggesting that these two quantities are useful for seismic monitoring and prediction. Here we study the relationship between these two quantities for different fluid injections carried out in the Soultz-sous-Forêts enhanced geothermal systems reservoir to see if it remains similar despite the changes and setting in the injection strategy (flow-rate, pressure of the injected fluid) and depths. Based on a harmonized database, we show that the ratio between the radiated seismic energy and hydraulic energy is at first order constant in time during stimulations and of the same magnitude independently of the stimulation strategy and depth. This ratio can then be seen as an intrinsic large-scale reservoir property that can be estimated from the early stages of the first stimulation. Using this reservoir property, we propose a method for predicting the maximum magnitude of induced seismic events given the maximum hydraulic energy planned.

1. Introduction

A seismic response to fluid injection has been widely observed in most enhanced geothermal system (EGS) reservoirs, whether during reservoir stimulation phases (permeability enhancement) or to a lesser extent during circulation test phases or during the exploitation phase (e.g., Majer et al., 2007; Zang et al., 2014). This seismicity can either be entirely controlled by anthropological activity (induced seismicity) or partially controlled by the tectonic loading of the reservoir (triggered seismicity). Although induced seismicity is generally of low magnitude ($M_L < 2$), exceptional events of greater magnitude can occur (at a relatively shallow depth). These events can be felt by the local population and can cause damage the local infrastructures (e.g., Giardini, 2009; Lee et al., 2019), which raises questions about the societal acceptance of such projects and potentially hindering the development of this renewable energy (Wüstenhagen et al., 2007). In order to mitigate the resulting seismic hazard, it is crucial to understand the factors that control the maximum magnitude of earthquakes resulting from the injection of fluids into deep fractured reservoirs. To predict the maximum magnitude of induced earthquakes, several authors have designed physics-based and probabilistic models that highlight the potential controlling factors. The first parameter that has been evidenced is the total fluid volume injected. Indeed, a proportional relationship between the maximum magnitude and the total volume of fluid injected has been observed on several EGS projects (e.g., Zang et al., 2014). McGarr (2014) showed that the two quantities can be related by assuming a proportional dependence of the seismic moment on the stimulated volume. Indeed, the injected fluid causes a

Writing – original draft: K. Drif
Writing – review & editing: K. Drif,
O. Lengliné, J. Kinscher, J. Schmitbuhl

deformation in the stimulated volume due to poro-elastic effect. This deformation is estimated using the effective elastic reservoir parameters and the friction coefficient on the reservoir faults. McGarr and Barbour (2018), then developed this approach to show that part of the calculated moment can be released during aseismic slip events. Similarly, Hallo et al. (2014) proposed to introduce a ratio between the released moment and the theoretical scalar cumulative moment as predicted from the injected volume and as defined by McGarr (2014). This ratio is intended to take into account aseismic deformation or inelastic effects within the reservoir, although they acknowledge that the physical model giving rise to the specific value of this ratio is still poorly understood. By introducing this new approach, they more accurately predict the total seismic moment associated with fluid injections, as well as the maximum possible magnitude.

Li et al. (2022) have revisited the approach of Hallo et al. (2014) by considering that at any time during injection, the ratio between the predicted and the observed cumulative seismic moment constitutes a stored energy that can be released in a single large event. By using this method, they are able to update this ratio continuously during injection and deduce the maximum expected magnitude.

In a different approach Shapiro et al. (2010) and Dinske and Shapiro (2013), introduced a relationship between the injected volume and the number of induced earthquakes by combining Gutenberg-Richter statistics with reservoir properties characterized by the seismogenic index. The seismogenic index is supposed to represent mainly the earthquakes magnitude distribution and the poro-elastic compliance of the stimulated reservoir.

In a later work, Van der Elst et al. (2016) used this seismogenic index to estimate the maximum magnitude. They demonstrated that the maximum magnitude is controlled by the regional tectonics, the connectivity of faults and above all, by the number of induced events. Thus, according to this model, the volume injected has more influence on the total number of induced seismic events than on the total seismic moment released.

In contrast to such a probabilistic approach, Galis et al. (2017) introduced a deterministic physic-based approach simulating the maximum rupture size of a fault depending on the pore pressure perturbation. They also found a relationship between the maximum possible magnitude and the injected volume. However, the maximum magnitude is controlled by a single fault, rather than a population of interconnected faults as in McGarr (2014) and Van der Elst et al. (2016).

Recent attempts have been made to compare the hydraulic energy related to the forced fluid injection and the radiated energy from induced seismicity in order to identify hazardous reservoir behavior (Bentz et al., 2020; Grigoli et al., 2018; Kwiatek et al., 2019). Kwiatek et al. (2019) and Bentz et al. (2020) investigated the usefulness of the hydraulic energy (product of fluid injection pressure and injection rate) in relation to the seismic response of the reservoir. Indeed, the forceful injection of water into the rock mass is associated with an energy transfer that is partially relaxed during faulting. The hydraulic energy was notably found to be well correlated with the seismic moment or the radiated seismic energy (Baujard et al., 2014; De Barros et al., 2019; Kwiatek et al., 2018) during fluid injection experiments. In particular, Kwiatek et al. (2019) demonstrated the usefulness of real-time continuous monitoring of the evolution of the seismic injection efficiency I_E , defined as the ratio of radiated seismic energy to hydraulic energy, for maintaining a low level of induced seismicity during an injection. The same approach was then used by Bentz et al. (2020) to study the evolutionary trends of I_E of 10 different geothermal projects. Their results showed that I_E can span many orders of magnitude (from 10^{-8} to 1) but remains nearly constant during a fluid injection. They proposed that this ratio is likely governed by reservoir parameters (e.g., the characteristic length of the reservoir's faults, their orientation and frictional properties). Furthermore, the authors argued that the monitoring of I_E during an injection can capture the transition of the reservoir from a stable to unstable state. This might be a good indicator for identifying an hazardous evolution preceding the occurrence of large events.

Following the approach of Kwiatek et al. (2019) and Bentz et al. (2020), we here aim at comparing the hydraulic energy associated with fluid injection and the energy released by induced earthquakes, but focusing on a single geothermal site with different injection operations and configurations (flow rate, injection pressure, injection depth). Indeed, rather than comparing measurements at several geothermal sites, this allows us to investigate the effect of the physical injection parameters (flow rate, pressure, injection depth, etc.), all other things being equal. In particular, we can analyze the effect of re-stimulation phases (i.e., stimulations carried out in a previously stimulated part of the reservoir). We chose the Soultz-sous-Forêts (France) site as a case study since it has a long history and an extensive database. Thus, 13 fluid injection episodes (for which data are available) are used and

compared. In order to avoid potential bias in our comparative analysis related to changes in the seismic and hydraulic network configuration and processing schemes, we perform a comprehensive data harmonization step, which focused on the consistent estimation of seismic moments. This has not yet been done, as the seismological studies carried out on the Soultz-sous-Forêts site have only focused on a few specific fluid injection operations (e.g., Cuenot et al., 2006; Charléty et al., 2007; Dorbath et al., 2009). In addition, unlike many other geothermal sites, the Soultz-sous-Forêts stress field has been estimated (Cornet et al., 2007). This allows us to use information, independent of seismic measurements to quantify the seismic energy released by induced seismicity. For this reason, in addition to radiated seismic energy, which only uses seismic data, we also propose to quantify the potential deformation energy released during faulting (seismic faulting energy).

After a description of the geothermal site of Soultz-sous-Forêts (Section 2), we present the compilation and harmonization of the seismological and hydraulic data relating to the various injections carried out in the reservoir (Section 3) and we analyze the evolution of the seismic moment and the observed maximum magnitudes with injected fluid volume and hydraulic energy (Section 3.3). We then define and present the values of the seismic injection efficiency, the seismic faulting energy and the seismic faulting efficiency which is a ratio analogous to I_E , but based on the seismic faulting energy (Section 4). Finally, we discuss their values and evolutions during injection as well as their implication in predicting maximum earthquake magnitude (Section 5).

2. Soultz-Sous-Forêts Site Features

2.1. Hydraulic Stimulations and Circulation Tests

The EGS project of Soultz-sous-Forêts, located in the central part of the Upper Rhine Graben, was initiated in 1984 (Gérard et al., 1984). Before becoming an industrial geothermal power plant in 2016, the project was under development for over 20 years (Genter et al., 2010; Schill et al., 2017). The geothermal reservoir has been developed in the granitic rock massif which is covered by sediment deposits of 1.4 km thickness (Vidal et al., 2015). The reservoir includes two different levels: the level R3 (between 1.4 and 3.9 km depth) characterized by a highly altered and fractured potassium feldspar granite and the level R5 (below 3.9 km depth) characterized by a fine-grained two-mica granite (Dezayes et al., 2005; Schill et al., 2017).

During the development phase, four wells were drilled and a series of hydraulic stimulations and circulation tests were carried out through different wells crossing the reservoir (see Figure 1) at the two depth levels R3 (around 3 km depth where temperature is around 160°C) and R5 (around 5 km depth where temperature is around 200°C). In 1986, the first well GPK1 was drilled up to 2 km deep and then extended to level R3 in 1992. In 1993, a hydraulic stimulation was performed in this well in two phases (September and October). In 1995, the second well, GPK2 was drilled at the same depth interval where two hydraulic experiments have been carried out: a first hydraulic stimulation in 1995 followed by a second hydraulic stimulation in 1996 of the same zone (re-stimulation). A fluid circulation between the wells GPK1 and GPK2 was then carried out in 1997. In 1999, the GPK2 well was extended to reach the level R5 followed by a hydraulic stimulation in 2000. As the project then developed, in 2002 and 2004, two new wells, namely GPK3 and GPK4, were drilled down to the reservoir R5 respectively. In 2003, the GPK3 well was used to stimulate the reservoir followed by a circulation test between the GPK2 and GPK3 wells. A stimulation and re-stimulation were then performed in the GPK4 well in 2004 and 2005, respectively. These final stimulations were then followed by a series of circulation tests involving GPK2, GPK3, and GPK4 in 2005 and all the four wells in 2008, 2009, and 2010.

All these hydraulic stimulations and circulation tests were monitored by a seismic monitoring network, but it changes significantly in time and space in terms of network geometry, instruments, and applied processing schemes used to generate the seismic catalogs (see Table S3 in Supporting Information S1 and Section 3.2.1 for a description of the seismic network evolution). The seismic and hydraulic data of these operations are for most of them archived and distributed in form of “episodes” by the Data Center for Deep Geothermal Energy (CDGP; <https://cdgp.u-strasbg.fr/>) but also by the EPOS TCS-AH platform (European Platform Observing System for Anthropogenic hazards; <https://tcs.ah-epos.eu/>). Each episode refers to a specific, time-limited, hydraulic operation carried on the reservoir.

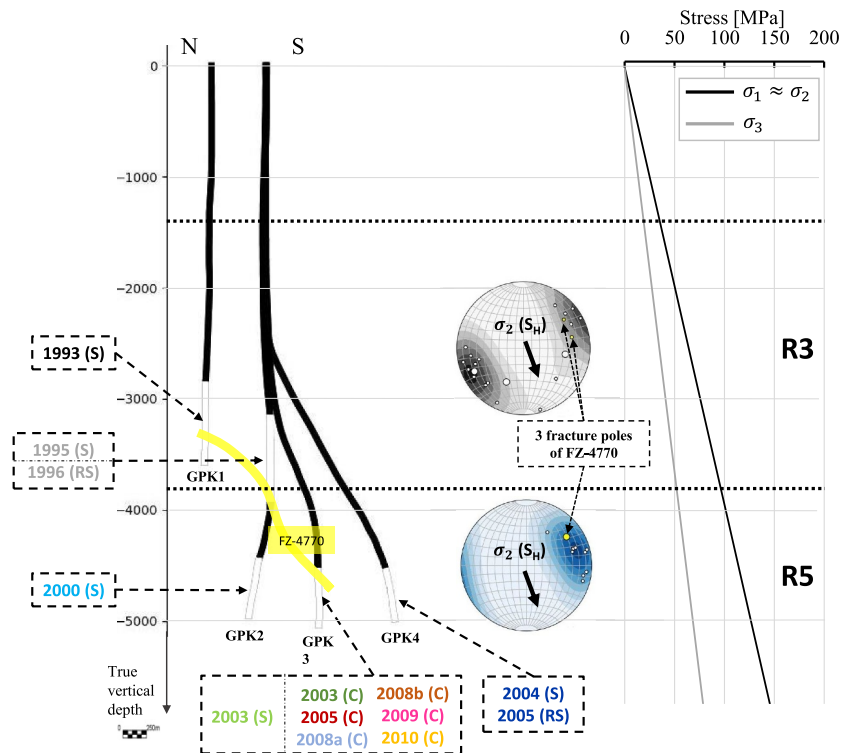


Figure 1. N-S section in depth with the four wells of the Soultz-sous-Forêts geothermal reservoir (GPK1, GPK2, GPK3, and GPK4) and the state of stress as a function of depth (σ_1 , σ_2 , and σ_3 are respectively the vertical stress, the maximum horizontal stress and the minimum horizontal stress). The horizontal lines represent the limits of the sub reservoirs R3 and R5 (Schill et al., 2017). Black arrows point the open-hole section of the injection well for the respective injection episode (stimulations: S, re-stimulations: RS and circulation tests: C). Circulation tests that involved two injection wells (i.e., 2009 and 2010) are shown here with an arrow pointing only to the injection well with the largest injected volume. The thick yellow line represents the major fault plane FZ-4770 intersecting GPK1, GPK2, and GPK3 (Sausse et al., 2010). For each reservoir, the direction of the maximum horizontal regional stress ($N170^\circ \pm 10^\circ$, Cornet et al., 2007) is represented. Fracture distribution evidenced by Dezayes et al. (2010) are represented by their poles in two stereonets. The fracture poles with larger circles correspond to major fractures which were already permeable before any stimulation and which were detected during drilling (significant mud losses). The fracture poles of the major fault FZ-4770 are represented as a yellow circle in the stereonets.

2.2. Structural Properties and Stress State of the Reservoir

The pre-existing fractures and the stress state of a reservoir play important roles in induced earthquakes by fluid injection. Fractures provide pathways for the fluid diffusion and reduce rock strength, while stress state determines the stability of the fractures under different pore pressure conditions. Indeed, fluid injection can increase the pore pressure within the fractures and faults, which reduces the effective normal stress and increases the shear stress acting on them. This can make them more prone to slip and generate seismicity (e.g., Ellsworth, 2013; Pearson, 1981). In a seismic analysis, it is therefore important to know the structural properties and stress state of the concerned reservoir.

The structural reservoir model at Soultz-sous-Forêts was mainly derived from borehole observations obtained from direct (cores, cuttings) and indirect (borehole images, geophysical logs, flow logs, temperature logs) methods (mainly acoustic borehole images). From this data, Dezayes et al. (2010) characterized the 39 main fracture zones intersecting the wells (see Figure 1 and the caption for more details). The orientation of these identified fracture zones are shown for the different reservoir level R3 and R5 in stereonets. The largest fracture zone FZ-4770 (see the yellow line in Figure 1) intersects the open-hole section of GPK1 (stimulated in 1993), the former open-hole section of GPK2 (stimulated in 1995 and 1996) and the GPK3 well just above its open-hole section (stimulated in 2003 and used as an injection well for all the circulation tests studied in this paper)

(Sausse et al., 2010). The dominant strike direction of the fracture zones in the granite of both R3 and R5 is $N160^{\circ}E \pm 10^{\circ}$ which is nearly similar to the orientation of the inferred maximum horizontal stress at the same level, $N170^{\circ} \pm 10^{\circ}$ (Cornet et al., 2007). The tectonic faulting regime in both reservoirs is mainly normal with a more or less pronounced strike-slip component as the vertical stress and the maximum horizontal stress are almost identical (Cornet et al., 2007; Meixner et al., 2016). This stress state is confirmed by the focal mechanisms of recorded earthquakes linked to injection phases which evidenced mostly normal or strike-slip faulting (Cuenot et al., 2006).

The deep regional stress field proposed by Cornet et al. (2007) is:

$$\sigma_1 = 33.8 + 0.0255(z - 1377) \quad (1)$$

$$\sigma_2 \simeq \sigma_1 (N170^{\circ} \pm 10^{\circ}) \quad (2)$$

$$\sigma_3 = 0.54\sigma_1 \quad (3)$$

$$p = 0.9 + 0.0098z \quad (4)$$

where z is the depth (in meters), p the pore pressure, σ_1 , σ_2 , and σ_3 are the principal stresses, with σ_1 the vertical stress, σ_2 the maximum horizontal stress and σ_3 the minimum horizontal stress. All stresses and pressure are given in MPa (see Figure 1).

2.3. Seismic Response of the Soultz-Sous-Forêts Reservoir

Induced earthquakes have been observed during all injections in the Soultz-sous-Forêts reservoir (Charl  ty et al., 2007; Cuenot et al., 2008; Dorbath et al., 2009). Earthquakes are less numerous during circulation although they can reach similar level of magnitude as in simulations (Cuenot et al., 2011). In most cases the onset of the seismic activity coincides with the start of injection except for stimulations of an already stimulated part of the reservoir as seismicity only occurs after a certain injected fluid pressure has been reached. This has been explained as a consequence of the Kaiser effect (e.g., Gaucher & Kohl, 2014). The seismicity observed during stimulations is mainly located around the openhole section of the injection well for both R3 and R5 stimulations (Baria et al., 2004; Cornet et al., 1997). The seismic cloud extends as the injection progresses in the direction of the favorably oriented faults within the stress state (Cuenot et al., 2008; Dorbath et al., 2009). Generally, seismic events migrate first to the lower part of the reservoir and then move upwards to shallower depths (Baria et al., 2004; Cauchie et al., 2020; Cuenot et al., 2008). Due notably to pore pressure diffusion mechanisms (e.g., Mukuhira et al., 2017) or aseismic slips (e.g., F. H. Cornet, 2016; Lenglin   et al., 2017), the seismic activity does not stop as soon as injection stops but continues with a decreasing rate after injection has stopped. As a consequence, the largest earthquake of the sequence is often recorded during this post shut-in phase (e.g., Charl  ty et al., 2007; Evans et al., 2012; Gaucher et al., 2015). It was proposed that the seismic response of the reservoir during stimulation is more important in terms of cumulative seismic moment for the deeper reservoir R5 than the shallower reservoir R3 (Bentz et al., 2020). Indeed, the cumulative seismic moment of the 2000 and 2003 stimulations seems to be three orders of magnitude higher than that of the 1993 stimulation, for the same volume injected. This is interpreted by the authors as a possible consequence of the difference in local tectonic features between the two depths for example, the length, the orientation or the frictional properties of faults.

In addition to the seismic response of the reservoir, fluid injection has been evidenced to produce aseismic slips in the Soultz-sous-For  ts reservoir. Indeed, there are some observational evidences and physical arguments that support the presence of aseismic slip in the two parts of the reservoir during stimulation experiments. For example, Cal   et al. (2011) and Cal   and Dorbath (2013) analyzed variations in P-wave velocity during the 2000 and 2003 stimulation episodes carried out in R5. They observed some velocity anomalies that they attributed to the occurrence of aseismic motion during these two episodes. In R3, Cornet et al. (1997) evidenced a 4 cm slip on a fault intersecting the GPK1 borehole around 3,000 m deep during the 1993 injection. This 4 cm slip could not be linked to any single seismic event. Assuming typical scaling laws (e.g., Madariaga, 1976), this 4 cm slip translates into a $M_w 3.5$ event but no such large magnitude earthquake was recorded during the injection. The occurrence of such aseismic motion was later confirmed by Bourouis and Bernard (2007) who analyzed repeating earthquakes

occurring on the identified fault plane hosting this large aseismic motion. They obtained a cumulative slip estimate from repeating earthquake of the same order of magnitude as the one reported in Cornet et al. (1997) from direct log comparisons.

3. Compilation and Harmonization of the Soultz-Sous-Forêts Inter-Episodic Database

3.1. Hydraulic Data Compilation

3.1.1. Presentation of Hydraulic Data

Hydraulic data of the Soultz-sous-Forêts site comprises the well-head pressure and the flow-rate measurements as a function of time for each stimulation and circulation episode (see Section 2). Hydraulic data used here for all the stimulation episodes and the 2003 and 2010 circulation test episodes are provided by the CDGP (<https://cdgp.ustrasbg.fr/>). For these episodes, we compiled and downsampled the data to a one-hour sampling in order to relate and compare hydraulic and seismological data in the same time series. For the five other circulation test episodes (i.e., from 2005 to 2010), no time series data were available. We used flow rate and well-head pressure from figures presented in Cuenot et al. (2011). This prevents us from obtaining an evolution of these hydraulic parameters over time but still yields integrated values over the whole episode. A summary of the injection configuration and hydraulic characteristics of each episode is documented in Table S1 in Supporting Information S1. We also track the temporal evolution of the wellhead fluid flow-rate and fluid pressure respectively during the injection operations (see Figure S1 in Supporting Information S1).

3.1.2. Hydraulic Energy Computation

Hydraulic energy is here defined as the mechanical energy injected into the reservoir through the pressurized fluid during a specific episode. This quantity takes into account both pressure and flow-rate evolution during injection. We note that this energy is estimated at the surface such that it represents a proxy of the mechanical perturbation created in the reservoir by the injection. Thus, hydraulic energy is here estimated from:

$$\Delta W_H = \int_0^{V_f} P(V)dV \quad (5)$$

where P is the injection wellhead pressure of the fluid and V is the injected fluid volume from 0 to the final injected volume V_f . This can be rewritten as a time integral covering the whole episode of fluid injection, between time t_i and t_f as

$$\Delta W_H = \int_{t_i}^{t_f} P(t)Q(t)dt \quad (6)$$

with Q the injection wellhead flow rate and $V(t_i) = 0$, $V(t_f) = V_f$. If a significant amount of fluid is pumped out of the reservoir at the same time of the injection, during an hydraulic circulation for example, the hydraulic energy in the reservoir is only the net hydraulic energy such that we need to subtract the energy of the production wells from the hydraulic energy of the injection wells that is,:

$$\Delta W_H = \Delta W_H^{in} - \Delta W_H^{out} = \int_{t_i}^{t_f} (P^{in}(t)Q^{in}(t) - P^{out}(t)Q^{out}(t)) dt. \quad (7)$$

Since only well-head measures are considered for injections at different depths, Equations 6 and 7 do not account for energy loss due to the dissipation of the mechanical energy of the fluid by friction with casing walls and by temperature effects (that can cause e.g. a loss of internal energy or a change in the fluid viscosity). In order to exclude such bias in our analysis, we computed an estimate of the energy loss by considering the fluid friction with casing walls. The details of the calculations are presented in Text S2 in Supporting Information S1. Results of our calculation showed that this potential loss in energy is not more than 5% which makes it negligible for our considerations.

3.2. Seismological Data Compilation and Harmonization

3.2.1. Presentation of Seismological Data

The main features of the earthquake catalogs for the corresponding stimulation and circulation episodes used in this study are shown in Table S3 in Supporting Information S1. Earthquake catalogs for stimulation episodes are provided by the CDGP (<https://cdgp.u-strasbg.fr/>). Catalogs for stimulation episodes cover the entire injection period and list all the events detected by the network with their location and magnitude. Only two catalogs are available for the circulation episodes (i.e., 2003 and 2010). For the other circulation episodes, only the total event number as well as the magnitude and number of the largest events was available, but without precise timing nor location (Cuenot et al., 2011). It is noteworthy that the seismological catalog of the 2003 circulation test does not cover the whole injection period but only the first 17 days. To avoid excluding this episode from the analysis, we decided to consider these first 17 days for which both hydraulic and seismic data are available.

Just as the network has evolved over time, so has the seismological processing. The 1993, 1995, and 1996 stimulations were monitored by four downhole stations installed in existing boreholes (three accelerometers in wells 4,550, 4,601, and 4,616 at around 1,500 m depth and 1 hydrophone in EPS1 well at 2,075 m depth) and 18 temporary surface stations seismometers installed by the Ecole et Observatoire des Sciences de la Terre (University of Strasbourg). For the stimulation of GPK2 in 2000, the accelerometer in the well 4,616 was removed and the GPK1 well was equipped with a downhole hydrophone at 3,500 m depth. In addition, a fifth downhole accelerometer was installed at the bottom of a new observation well, OPS4, drilled down to around 1,500 m depth (Baria et al., 2006) and the 18 surface seismometers continued to record seismic activity. Since 2003, a permanent surface network of nine stations has been installed to continuously monitor seismic activity and one downhole geophone in the well 4,616 has been added at about 1,370 m depth. The permanent surface network was completed by 14 temporary seismometers for the 2003 injection operations and 4 temporary seismometers for the 2004 and 2005 operations (Charl ty et al., 2007; Cuenot et al., 2008). Given the characteristics of these stations, the seismic networks were able to detect small induced events (see Section 3.2.3) and to localize the events detected. However, the seismic network evolution over time is supposed to have significant impact on the network detection and location performance. A difficulty also arises when comparing the different simulations as one needs to make sure that the reported seismological data have all the same definition, and in particular earthquake magnitudes which are used to compute the seismic moment, M_0 . To overcome this difficulty, we have regrouped the episodes with the same reported magnitude definition into four groups:

- The earthquake catalogs corresponding to the 1993, 1995, and 1996 episodes have all been computed by the Camborne School of Mines Associates (CSMA), following the same approach (Jones, 1997). They estimated a moment for each detected earthquake by fitting a Brune's model to the earthquake spectrum (Brune, 1970). From these seismic moment estimates, they derived a magnitude, hereafter referred to as M_{CSMA} that cannot be considered as moment magnitudes in the sense of Hanks and Kanamori (1979) since they used a different equation to convert seismic moment into moment magnitude.
- The earthquake catalogs for the stimulation episode of 2000 and the circulation tests from 2005 to 2010 have all been compiled using the same methodology and all report a duration magnitude, M_D .
- The earthquake catalogs of the 2003 stimulation and circulation tests report a local magnitude that is a network based local magnitude, hereafter defined as M_L^1 .
- The earthquake catalogs of the 2004 and 2005 stimulation episodes report a local magnitude that is computed using the amplitude of the raw signal of one of the downhole sensor (4,550), hereafter defined as M_L^2 .

3.2.2. Harmonization to Moment Magnitude Scale

As a prerequisite for the energy analysis, the difference in magnitude scale between the earthquake catalogs (either CSMA, local or duration magnitudes) must be taken into account in order to obtain a fully homogeneous and comparable database of earthquake magnitudes. In this respect, we aimed to convert the magnitudes of each of these groups into seismic moments and associated moment magnitudes (Hanks & Kanamori, 1979). The conversion procedure consists of three main steps for each of the groups mentioned above: (a) direct estimation of seismic moments for events for which waveforms and instrument response were available; (b) establishment of an empirical relationship (based on a robust regression) between the computed seismic moments and the reported magnitudes; (c) estimation of seismic moments from the conversion relationships in (b) for all events that belong to the same group.

As part of the first step, seismic moments were calculated by fitting a Brune's model (Brune, 1970) to the observed S -wave displacement and acceleration spectra using the SourceSpec algorithm (Satriano, 2022). We fitted displacement spectra from seismometer data to the (3–50 Hz) frequency band and acceleration spectra from downhole accelerometers to the (80–500) Hz band. The best fit estimate returns for each event the seismic moment M_0 linked to the low-frequency plateau of displacement or acceleration amplitude spectra, Ω_0 . The theoretical displacement spectrum $u(f)$ is defined as:

$$u(f) = \frac{\Omega_0}{1 + \left(\frac{f}{f_c}\right)^2} \exp\left(\frac{-\pi r f}{Q_S V_S}\right) \quad (8)$$

where f_c is the corner frequency, r is the hypocentral distance, Q_S is the attenuation factor and V_S is the S -wave velocity (here $V_S = 3.34$ km/s, Jupe et al., 1994). The low-frequency plateau Ω_0 comprises the seismic moment M_0 and accounts for geometrical spreading, radiation pattern R_S (here assumed to be 0.63, Aki & Richards, 1980), S -wave velocity V_S and medium density ρ (here assumed to be 2,500 kg/m³) and is defined as:

$$\Omega_0 = M_0 \frac{R_S}{4\pi\rho V_S^3 r} \quad (9)$$

While f_c and Q_S estimates may be subject to large uncertainties, the low frequency part of the displacement spectrum is generally robust and thus M_0 can be reliably derived.

As part of the second and third steps, we obtained the following empirical relationships between the seismic moments and the reported magnitudes of each group:

- For the 1993, 1995, and 1996 simulation episodes, we estimated the seismic moment of all earthquakes in the 1993 catalog for which waveforms and instrument response are available (four downhole stations). Based on these results we established the following relationship between the initial catalogs magnitude M_{CSMA} and the seismic moment following regression analysis (see Figure S3a in Supporting Information S1):

$$M_0 = 10^{(1.72 \pm 0.01)M_{CSMA} + (11.04 \pm 0.02)} \quad (10)$$

This relationship was used to also deduce the seismic moments for the 1995 and 1996 stimulations. The resulting moment magnitudes are 1.4 magnitude units higher than those of M_{CSMA} . This is consistent with observations of Baisch et al. (2010) who noticed that M_{CSMA} appear unusually low by as much as two magnitude units compared to other moment magnitude estimates performed from surface instruments. It is noticeable that Jones (1997) reported a relation between moment and magnitude for CSMA catalog very similar to Equation 10 but with a factor of 1.1 instead of 11.04 which, based on our results is probably a typo.

- For the stimulation episode of 2000 and the circulation tests from 2005 to 2010, we similarly established a relationship between the duration magnitude scaled M_D and the seismic moment which reads as:

$$M_0 = 10^{(1.47 \pm 0.17)M_D + (8.22 \pm 0.34)} \quad (11)$$

The adjustment was performed only for events with $M_D > 1.25$ (data quality was poorer for lower magnitudes) of the episodes of 2000 and 2010 (no waveform data are available for the other circulation tests). Given the difference in the seismic network, we independently inverted two conversion relations on both the data from the 2000 stimulation (16 surface stations) and the data from the 2010 circulation test (six surface stations). These relations were found to be nearly similar. Because the 2010 episode contains less data, we retained the one inverted on the 2000 stimulation (see Figure S3b in Supporting Information S1) to deduce seismic moment of each episode (including the 2005, 2008, and 2009 circulation tests for which no waveform data were available).

Table 1
Description of the Harmonized Seismic Catalogs for Each Stimulation and Circulation

Episode	M_W^c	$\log_{10}(\Sigma M_0(M_W \geq M_W^c))$ M_0 in (N m)	$\log_{10}(M_0^{\max})$ M_0 in (N m)	M_W^{\max}
Stimulation				
1993 ^a	-0.65	13.12 ± 11.59	12.40 ± 0.01	2.20 ± 0.01
1995	0.05	12.90 ± 11.38	11.23 ± 0.01	1.42 ± 0.01
1996	0.05	13.22 ± 11.69	11.57 ± 0.01	1.65 ± 0.01
2000	-0.45	13.38 ± 13.28	11.90 ± 0.34	1.86 ± 0.22
2003	-0.05	13.12 ± 12.28	11.77 ± 0.08	1.78 ± 0.05
2004	-0.55	12.94 ± 12.71	10.93 ± 0.27	1.22 ± 0.18
2005	-0.45	12.86 ± 12.64	10.93 ± 0.27	1.22 ± 0.18
Circulation tests				
2003 ^b	-0.05	11.57 ± 10.66	10.66 ± 0.06	1.03 ± 0.04
2005 ^c	-	12.38 ± 12.29	11.60 ± 0.32	1.66 ± 0.21
2008a ^c	-	11.35 ± 11.18	10.28 ± 0.25	0.78 ± 0.17
2008b ^c	-	11.04 ± 10.89	10.72 ± 0.27	1.08 ± 0.18
2009 ^c	-	11.36 ± 11.24	10.72 ± 0.28	1.08 ± 0.18
2010	-0.25	12.23 ± 12.18	11.60 ± 0.32	1.66 ± 0.21

Note. M_W^c is the moment magnitude of completeness, $\Sigma M_0(M_W \geq M_W^c)$ is the 95 % confidence interval (CI) of the sum of the seismic moment of the events whose the magnitude is above the completeness magnitude M_W^c , M_0^{\max} is the 95 % CI of the maximum seismic moment observed for the largest magnitude M_W^{\max} event. The 95 % CI have been computed using a monte carlo approach on the parameters and associated uncertainties of the conversion relations. ^aHere we only analyze the injection phase of September 1993. ^bThe available seismological catalog does not cover the 2 months duration of the circulation tests but only 17 days. We therefore consider hydraulic data for these 17 days as well. ^cEpisodes for which seismological and hydraulic data were not available and for which we have derived values from Cuenot et al. (2011).

- For the 2003 stimulation and circulation episodes, we computed the seismic moments from the available waveforms of the 2003 stimulation episode (16 surface stations) and fitted (see Figure S3c in Supporting Information S1) the following relationship between the local magnitudes M_L^1 (above 0.5 to improve the accuracy) and the seismic moments:

$$M_0 = 10^{(0.98 \pm 0.04)M_L^1 + (8.96 \pm 0.07)} \quad (12)$$

This relationship is very similar to that obtained by Douglas et al. (2013) for the 2003 stimulation episode.

- For the 2004 and 2005 local magnitudes, we computed the seismic moments from the available waveforms of the 2004 stimulation episode (two surface stations) and fitted (see Figure S3d in Supporting Information S1) the following relation between these local magnitudes M_L^2 (above 1.3 to improve the accuracy) and the seismic moments:

$$M_0 = 10^{(0.77 \pm 0.15)M_L^2 + (9.16 \pm 0.28)} \quad (13)$$

Although the regressions were performed over a limited range of magnitudes (i.e., $M_D > 1.25$; $M_L^1 > 0.5$; $M_L^2 > 1.3$), we have included in our analysis the seismic moments of lower magnitude events, considering that the relationships obtained remain valid at lower magnitudes.

3.2.3. Catalog Completeness

Based on the inferred harmonized moment magnitudes, we deduced the magnitude of completeness, M_W^c for each episode. This allows differences in network detection performance to be taken into account. M_W^c was estimated by using the goodness of fit method (Wiemer & Wyss, 2000). We then computed the cumulative seismic moment

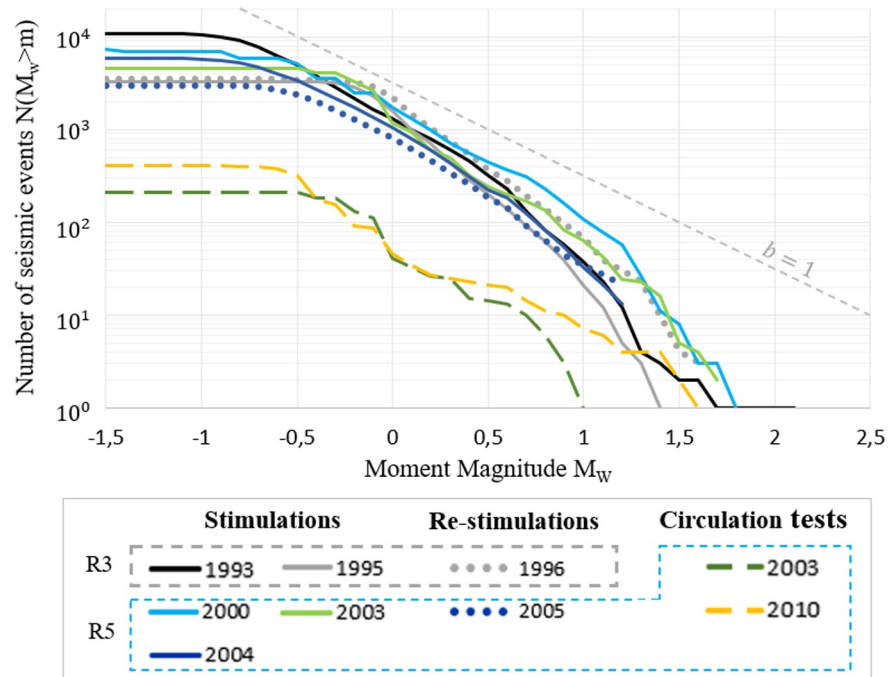


Figure 2. Cumulative frequency distribution of the moment magnitude of all events for the various episodes. The gray dotted line indicates a Gutenberg-Richter distribution for a b -value of 1. The black and gray curves refer to the injections in R3, while the colored curves refer to those in R5.

$\Sigma M_0(M \geq M_c)$ for each stimulation and circulation episode as the sum of the seismic moment of each recorded earthquake in the catalog whose magnitude is greater than or equal to M_w^c (see Table 1). Based on our estimates of M_w^c , we used the earthquakes magnitude distribution (Gutenberg & Richter, 1944; Figure 2) to compute the deficit in recorded seismic moment. The detailed procedure is explained in Supporting Information S1 (see Text S4). Similarly to the conclusions of Bentz et al. (2020), we find that the missing seismic moment accounts for a negligible amount compared to the seismic moment of events above M_c .

3.3. Cumulative Seismic Moment Evolution With Hydraulic Energy

We computed cumulative seismic moment ΣM_0 for each injection episode. In order to get a first overview of our compiled data set, we represent in Figure 3 the evolution of ΣM_0 with hydraulic energy ΔW_H . Based on our harmonized database, we show that, despite differences between episodes in terms of injection strategy and depth, the cumulative seismic moments are of similar order (between 7×10^{12} and 2×10^{13} N m) at similar hydraulic energy level (between 2×10^{11} and 6×10^{11} J) for stimulations. The cumulative seismic moment increases almost linearly with hydraulic energy for stimulations. We evidence a specific behavior for re-stimulations for which the onset of the seismic moment increase occurs only late during the injection and then rises sharply. At the end of the re-stimulation we note however, that the total seismic moment and maximum magnitude are very similar to the preceding stimulation. In addition, circulation tests globally show cumulative seismic moments of around one order of magnitude lower than for stimulations (between 1×10^{11} and 2×10^{12} N m) whereas hydraulic energies were higher (between 1×10^{11} and 2×10^{12} J). Similarly to re-stimulations, circulation tests show a strong non-linear increase of the cumulative seismic moment with hydraulic energy but this evolution becomes almost linear after a certain level of hydraulic energy injected.

4. Measuring the Seismic Energy Released

During slip on a pre-existing fault the potential energy change, ΔW_{fault} , is generally decomposed into fracture energy, E_G , thermal energy (frictional), E_{TH} , and radiated seismic energy, E_R . The fracture energy or breakdown work actually encompass a variety of inelastic processes occurring both on and off-fault (Kanamori & Brodsky, 2004; Udías et al., 2014). The thermal energy is commonly associated with frictional heating. The last term,

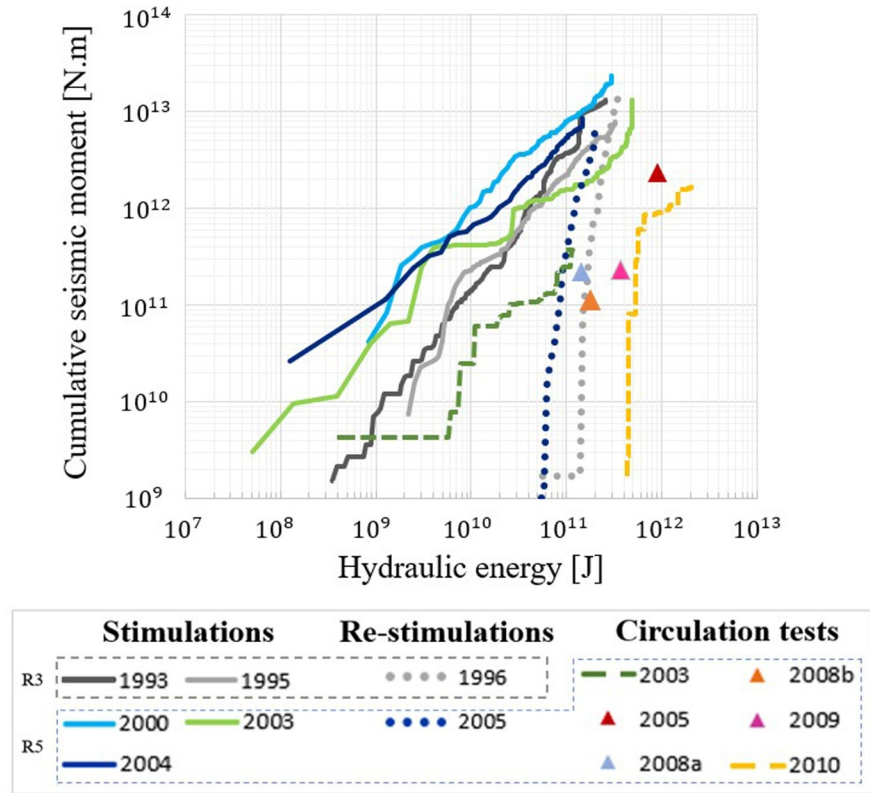


Figure 3. Cumulative seismic moment evolution with hydraulic energy injected. The black and gray curves refer to the injections in R3, while the colored curves refer to those in R5. Since we do not have a full data set for the 2005 to 2009 circulation tests, they are here represented as single values only at the end of the episode (triangle symbols).

E_R is linked to the radiation of seismic wave and is one of the most fundamental measures to understand the physical phenomenon associated with earthquake dynamics (see e.g. Gutenberg & Richter, 1956; Kanamori et al., 1993). E_R is found to be very small compared to the ΔW_{fault} (Kanamori et al., 2001) as the ratio $\eta = E_R / \Delta W_{fault}$, called the seismic efficiency, is typically lower than 6% (McGarr, 1999). The relative proportion $\eta_R = E_R / (E_R + E_G)$, the radiation efficiency, changes with the rupture speed and tends to 0 for quasi-static rupture (Husseini & Randall, 1976). Overall, the coefficients η and η_R can vary between events, reflecting the diversity of the rupture process. In our study, we first seek to estimate and compare E_R and its link with hydraulic energy that is, the seismic injection efficiency I_E for all injections in the Soultz-sous-Forêts reservoir. We show that, from an estimate of the stress state in the reservoir, we obtain an estimate of the seismic faulting energy. This offers a complementary characterization of the reservoir seismic response that shares similarities with I_E .

4.1. Radiated Seismic Energy and Seismic Injection Efficiency

The estimation of seismic injection efficiency, I_E has been studied in some previous works (Bentz et al., 2020; Kwiatek et al., 2019) and is defined as the ratio between the radiated seismic energy E_R and the hydraulic energy ΔW_H :

$$I_E = E_R / \Delta W_H, \quad (14)$$

where E_R can be computed from

$$E_R = C\rho V_S \int_0^\infty v(f)^2 df, \quad (15)$$

Table 2

Computed Values of Hydraulic Energy ΔW_H , Radiated Seismic Energy E_R , Maximum Seismic Faulting Energy ΔW_{fault} , Seismic Injection Efficiency I_E and Seismic Faulting Efficiency χ for All Stimulations, Re-Stimulations (RS) and Circulations Tests

Episodes	ΔW_H (J)	E_R (J)	ΔW_{fault} (J)	I_E (-)	χ (-)
Stimulation					
1993 ^a	2.58×10^{11}	$(9.14 \pm 0.07) \times 10^8$	$(2.21 \pm 0.04) \times 10^{10}$	$(3.55 \pm 0.03) \times 10^{-3}$	$(8.57 \pm 0.17) \times 10^{-2}$
1995	3.24×10^{11}	$(5.49 \pm 0.24) \times 10^8$	$(1.57 \pm 0.06) \times 10^{10}$	$(1.70 \pm 0.07) \times 10^{-3}$	$(4.86 \pm 0.17) \times 10^{-2}$
1996 (RS)	3.45×10^{11}	$(9.65 \pm 0.09) \times 10^8$	$(3.30 \pm 0.11) \times 10^{10}$	$(2.79 \pm 0.03) \times 10^{-3}$	$(9.56 \pm 0.33) \times 10^{-2}$
2000	3.02×10^{11}	$(1.58 \pm 1.26) \times 10^9$	$(6.53 \pm 5.24) \times 10^{10}$	$(5.24 \pm 4.18) \times 10^{-3}$	$(2.17 \pm 1.74) \times 10^{-1}$
2003	4.83×10^{11}	$(8.74 \pm 1.26) \times 10^8$	$(3.46 \pm 0.50) \times 10^{10}$	$(1.81 \pm 0.26) \times 10^{-3}$	$(7.17 \pm 1.04) \times 10^{-2}$
2004	1.48×10^{11}	$(4.53 \pm 3.40) \times 10^8$	$(2.43 \pm 1.43) \times 10^{10}$	$(3.07 \pm 2.3) \times 10^{-3}$	$(1.65 \pm 0.97) \times 10^{-1}$
2005 (RS)	2.00×10^{11}	$(4.14 \pm 2.90) \times 10^8$	$(2.01 \pm 1.22) \times 10^{10}$	$(2.07 \pm 1.45) \times 10^{-3}$	$(1 \pm 0.61) \times 10^{-1}$
Circulation test					
2003	9.34×10^{10}	$(2.47 \pm 0.30) \times 10^7$	$(1.07 \pm 0.13) \times 10^9$	$(2.64 \pm 0.32) \times 10^{-4}$	$(1.14 \pm 0.14) \times 10^{-2}$
2005 ^b	9.58×10^{11}	$(1.59 \pm 1.33) \times 10^8$	$(6.95 \pm 5.81) \times 10^9$	$(1.66 \pm 1.39) \times 10^{-4}$	$(7.25 \pm 6.06) \times 10^{-3}$
2008a ^b	1.65×10^{11}	$(1.48 \pm 1.00) \times 10^7$	$(6.46 \pm 4.36) \times 10^8$	$(8.97 \pm 6.08) \times 10^{-5}$	$(3.92 \pm 2.65) \times 10^{-3}$
2008b ^b	2.00×10^{11}	$(1.51 \pm 0.54) \times 10^7$	$(3.29 \pm 2.36) \times 10^8$	$(3.77 \pm 2.7) \times 10^{-5}$	$(1.65 \pm 1.18) \times 10^{-3}$
2009 ^b	4.43×10^{11}	$(3.08 \pm 1.12) \times 10^7$	$(6.75 \pm 4.91) \times 10^8$	$(3.48 \pm 2.53) \times 10^{-5}$	$(1.53 \pm 1.11) \times 10^{-3}$
2010	1.75×10^{12}	$(2.23 \pm 0.96) \times 10^8$	$(5.00 \pm 4.30) \times 10^9$	$(6.4 \pm 5.5) \times 10^{-5}$	$(2.86 \pm 2.46) \times 10^{-3}$

^aConcerns the September 1993 injection phase only. ^bEpisodes for which we do not have a seismic catalog.

where ρ is the density, V_S is the shear wave velocity, $v(f)$ is the velocity spectra and C is a constant to account notably for source azimuthal averaging and geometrical spreading. Due to the band limitation of the recording instrument and uncertainties regarding adequate attenuation correction, station coverage, etc., the calculation of E_R faces a number of practical challenges that must be overcome in order to be measured accurately (Ide & Beroza, 2001; Shearer, 2019). As a consequence, E_R is often estimated from the seismic moment M_0 (Randall, 1972) as:

$$E_R = \frac{\Delta\sigma}{2\mu} M_0 \eta_R \quad (16)$$

where $\Delta\sigma$ is the stress drop, μ is the shear modulus and η_R is the radiation efficiency. Following Bentz et al. (2020), we compute E_R using Equation 16 assuming a typical stress drop $\Delta\sigma = 3$ MPa (McGarr, 2014) and $\eta_R = 0.46$ (McGarr, 1999). Considering that the Young's modulus of the granite in R3 and R5 is $E = 25$ GPa and that the Poisson's ratio in R3 and R5 is $\nu = 0.25$ and $\nu = 0.2$ respectively (Vallier et al., 2019), then the shear modulus is $\mu = 10$ GPa in R3 and $\mu = 10.4$ GPa in R5.

For each available episode we computed the radiated seismic energy E_R and the seismic injection efficiency I_E . The absolute values of these quantities at the end of each episode (i.e., after the last recorded event in the catalog of the considered episode) are reported in Table 2 and the evolutions with hydraulic energy are shown in Figure 4.

As a first observation, we notice that all episodes are characterized by low values of seismic injection efficiency I_E ranging between 3.4×10^{-5} and 5.2×10^{-3} . Generally, stimulations and re-stimulations are characterized by similar I_E values (between 1.7×10^{-3} and 5.2×10^{-3}) which are an order of magnitude higher than those of circulation tests (3.4×10^{-5} and 2.6×10^{-4}).

As in Figure 3, which shows cumulative seismic moment evolution as a function of hydraulic energy, we observe in Figure 4 a distinct pattern in the evolution of radiated seismic energy and I_E with hydraulic energy depending on the type of injection. Indeed, the evolutions of E_R or I_E as a function of ΔW_H are different for stimulation and re-stimulation episodes. The dashed lines showing a constant value of I_E for stimulations suggest that radiated

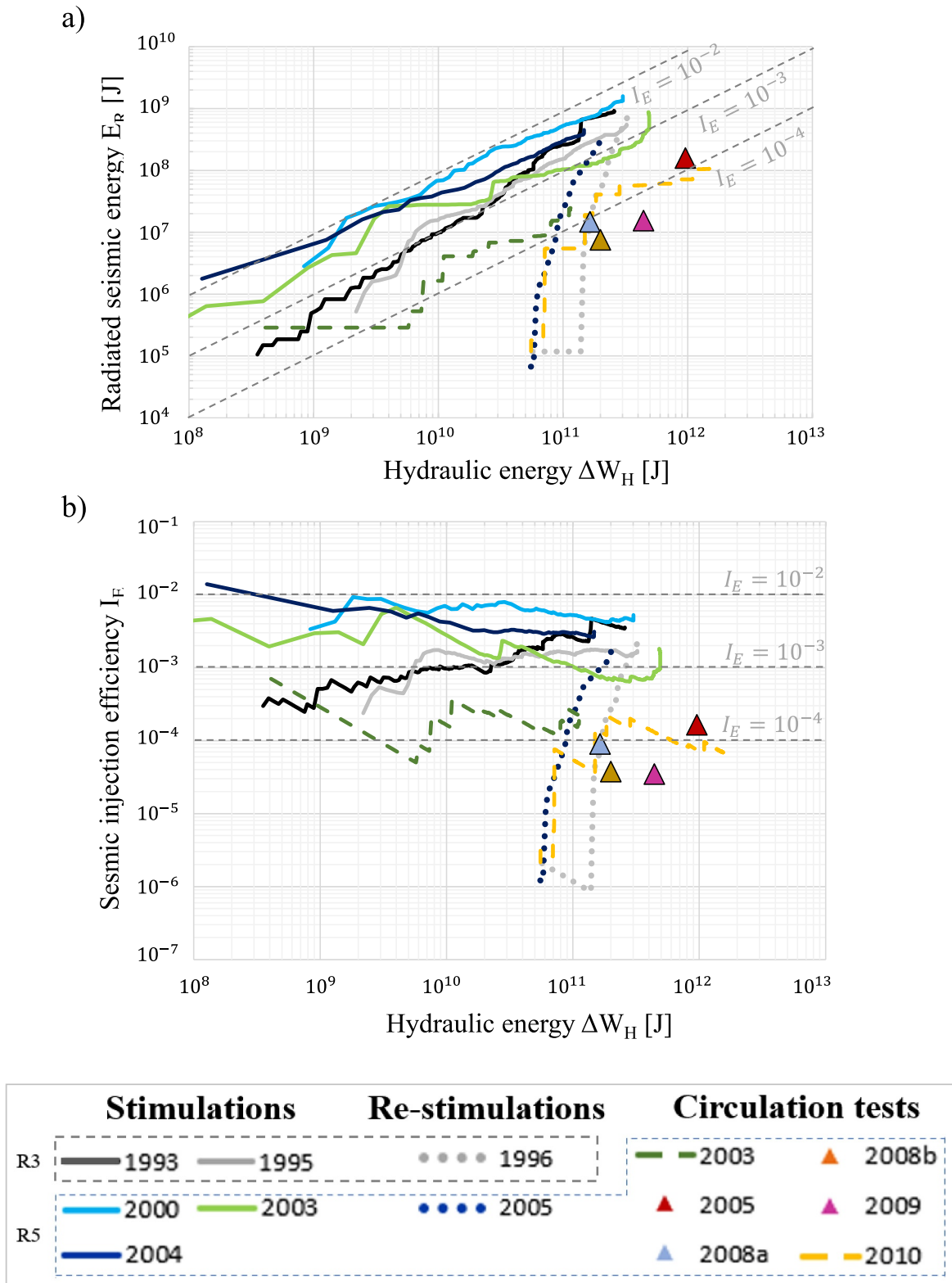


Figure 4. (a) Evolution of the cumulative radiated seismic energy E_R with hydraulic energy ΔW_H . (b) Evolution of the seismic injection efficiency I_E with hydraulic energy. The gray dotted lines show the linear evolution of the radiated seismic energy with hydraulic energy considering several constant values of seismic injection efficiency, I_E . Same color and marker codes as in Figure 3.

seismic energy increases almost linearly with hydraulic energy if we ignore small changes in I_E below one order of magnitude for certain stimulations (e.g., 1993 and 1995 stimulations) as seen in Figure 4b.

In contrast, the evolution of the seismic responses for re-stimulations differ significantly from the quasi-constant I_E as seen for stimulations. For these re-stimulation episodes, we notice a strong increase of I_E with the hydraulic energy that finally converges to similar values of I_E as observed from the preceding stimulation phases. This sharp increase is only observed after significant hydraulic energy (close to that injected during the previous stimulation) is injected into the reservoir (between 5×10^{10} and 8×10^{10} J). Regarding the circulation tests, Figure 4a represents the evolution of E_R for the circulation episodes in 2003 and 2010. We also observe in Figure 4b that I_E is almost constant for the 2003 circulation test as for stimulations. For the 2010 circulation test, a significant increase in I_E is comparable to those seen during re-stimulations.

Finally, our results do not highlight a significant difference between R3 and R5 in terms of I_E and cumulative seismic moments. This contrast with the results of Bentz et al. (2020) who show a difference of three orders of magnitude between both reservoirs in terms of cumulative seismic moment. They interpreted this difference as a potential result of the difference in reservoir depth (local tectonic features). The observed difference is likely related to a different estimation of the seismic moment. Indeed, it seems that Bentz et al. (2020) considered all the magnitudes in the CSMA catalog as moment magnitudes. However, as we showed previously and noticed by Baisch et al. (2010), the magnitudes reported in the CSMA catalog cannot be converted to seismic moment using the relation of Hanks and Kanamori (1979). This discrepancy in analysis highlights the importance of harmonizing data before a comparative analysis between different injection episodes at the same site, but also between different sites to avoid misleading interpretations.

4.2. Seismic Faulting Energy and Seismic Faulting Efficiency

As the state of stress is known in the Soultz-sous-Forêts reservoir, in addition to the previous estimate of the seismic radiated energy, we can quantify the variation in potential energy associated with the induced earthquakes in a different way. The change of potential energy during faulting (hereafter called seismic faulting energy), ΔW_{fault} , can be computed from

$$\Delta W_{fault} = DS \left(\frac{\tau_i + \tau_f}{2} \right) \quad (17)$$

with D the displacement on the fault, S the fault area and τ and τ_f are the shear stresses on the fault respectively at the start and at the end of the slipping episode (Kanamori & Brodsky, 2004; Knopoff, 1958; Kostrov, 1974). Introducing the seismic moment (Aki, 1966), one can rewrite Equation 17 as

$$\Delta W_{fault} = M_0 \left(\frac{\tau_i + \tau_f}{2\mu} \right). \quad (18)$$

We establish an upper estimate of the seismic faulting energy ΔW_{fault} , considering that the stress drop is found to be a small fraction of the total stress (Abercrombie, 2021). Setting $\tau_f = \tau_i$ then leads to a maximum energy, ΔW_{fault} that is twice larger than its minimum estimate ($\tau_f = 0$). From Equation 17 we have

$$\Delta W_{fault} = M_0 \left(\frac{\tau_i}{\mu} \right). \quad (19)$$

The initial shear stress, τ_i on the fault is generally unknown but can be estimated from stress field measurement. An upper estimate of the shear stress on the fault, τ_i^{\max} is given by $\tau_i^{\max} = \frac{\sigma_1 - \sigma_3}{2}$ where σ_1 and σ_3 are the maximum and minimum principal stresses (see e.g., Jaeger et al., 2009), which combined with Equation 19 yields

$$\Delta W_{fault} = M_0 \left(\frac{\sigma_1 - \sigma_3}{2\mu} \right). \quad (20)$$

This upper estimate of τ_i does not account for the fact that failure might occur at different levels of shear stress depending notably on the fault plane orientation and the friction coefficient and that it can vary as a function of

time because of stress transfer caused by nearby slip events. However, we can show that considering a fault plane ideally oriented for rupture and a fault friction coefficient of (0.6–0.9) the shear stress at failure will be in the range of (0.3–0.8) of the maximum shear stress which indicates that our maximum estimate is capturing the correct order of magnitude. As we are considering here a maximum fault energy scenario, it is therefore reasonable to have such an estimate of τ_p , but it should be noted that the shear stress at rupture could be less than this value and could change as a function of time.

We can then calculate the seismic fault energy as the sum of the seismic fault energy (Equation 20) of each event taking place during a fluid injection (see Table S3 in Supporting Information S1) using the seismic moment, the shear modulus and the principal stresses (introduced in Section 2) relevant to the depth of each of these events. Similarly to the injection efficiency, I_E , we can as well quantify the ratio between the seismic faulting energy and the hydraulic energy. We thus define, χ , the seismic faulting efficiency, as

$$\chi = \frac{\Delta W_{fault}}{\Delta W_H}, \quad (21)$$

and we note that I_E and χ are actually related and we have

$$\chi = \left(\frac{\sigma_1 - \sigma_3}{\Delta \sigma \eta_R} \right) I_E. \quad (22)$$

Assuming a constant stress drop, $\Delta \sigma$, and a constant radiation efficiency η_R , as done here, it implies that I_E and χ are related and only deviates from linearity because of the depth dependence of the principal stresses. Both, I_E and χ have a similar but slightly different meaning and each one carries its own uncertainties and assumptions. The radiated seismic energy estimate is based solely on seismic measurements. We note that the estimation of E_R based on Equation 15 is mostly dependent on the high frequency part of the signal as 80% of the seismic energy is radiated at frequencies above the corner frequency (Ide & Beroza, 2001). The estimation of E_R from Equation 16 also only involves seismic measurement as the estimate of stress drop is calculated from the same seismic data. For the seismic faulting energy, we rely on the stress field estimated from non-seismic measurements for an approximation of the initial stress (not for the final stress, for which we develop hypotheses). We also noted that $\Delta W_{faulting}$ and χ offer the opportunity to quantify the work done during an aseismic slip if we can estimate the seismic moment associated with such an event, which is not possible from I_E . Either I_E or χ can be calculated for monitoring the seismic response of the reservoir to fluid injection according to the seismological data available at the geothermal site. If the stress field is not known, it is not possible to calculate χ but I_E can be calculated. If the stress field is known, both I_E and χ can be calculated.

For each available episode, we computed the seismic faulting energy ΔW_{fault} and the seismic faulting efficiency, χ . The absolute values of these quantities at the end of each episode (i.e., after the last recorded event in the catalog of the considered episode) are reported in Table 2. Given Equation 22 and since we are comparing several injection episodes on the same site (same stress field), we can expect similar relative values and evolution of seismic radiated energy E_R and seismic faulting energy ΔW_{fault} (and hence I_E and χ). Indeed, Figure 5 representing the evolution of χ with I_E shows that I_E and χ are linearly related.

Hence, the observations made about I_E in the previous section remain the same for χ values. Indeed, all episodes are characterized by low values of χ ranging between 1.5×10^{-3} and 2.2×10^{-1} . This implies that the seismic faulting energy represents only a small part of the hydraulic energy. Similar values of χ are also observed between Stimulations and Re-stimulations (between 4.8×10^{-2} and 2.2×10^{-1}) which ranges one order higher than those for circulation tests (between 1.5×10^{-3} and 1.1×10^{-2}). Likewise, χ is almost constant during stimulation, whereas it increases strongly during re-stimulation to reach χ values similar to those observed during previous stimulation phases. Finally, no dependence of χ on injection depth is observed.

5. Discussions

5.1. Seismic Faulting Efficiency and Aseismic Slip

In our faulting energy estimation, we considered only the observed part of the faulting, that is, the part that radiates seismic waves and can be captured by a seismometer. It is likely that some faulting in the reservoir can also

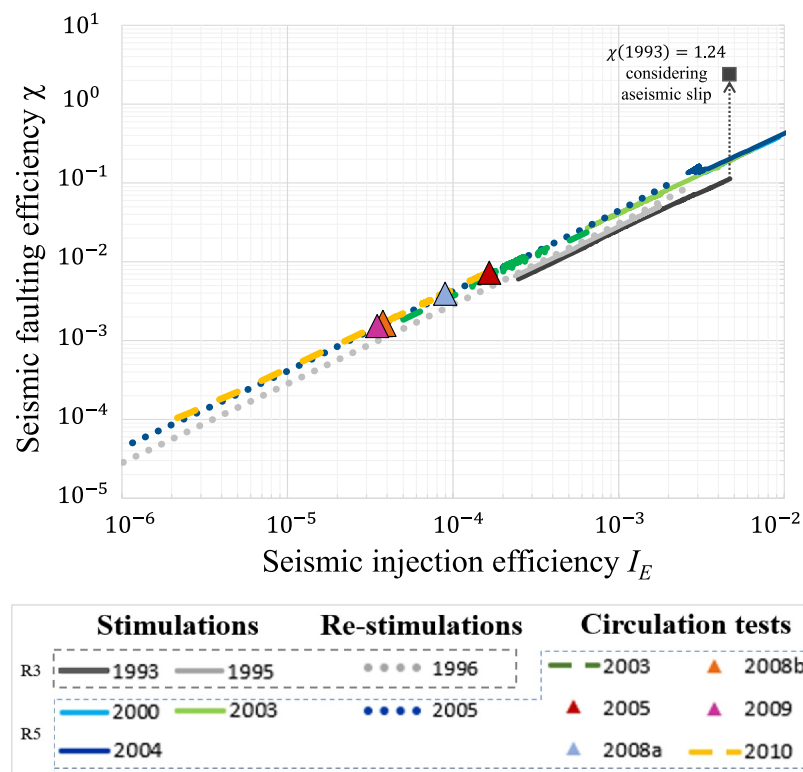


Figure 5. Relation between the seismic injection efficiency, I_E and the seismic faulting efficiency, χ . Same color and marker codes as in Figure 3.

be aseismic and thus are missed and not taken into account in our estimate of ΔW_{fault} . There are observational evidences and physical arguments that support the hypothesis of aseismic slip taking place in the two parts of the reservoir (see Section 2.3). A direct measure of aseismic slip was deduced from the 1993 stimulation by Cornet et al. (1997) and it was shown to be equivalent to a $M_w 3.5$ event ($M_0 = 2.04 \times 10^{14}$ N m). This value is significant compared to the cumulative seismic moment previously deduced for the whole 1993 episode (1.3×10^{13} N m). By accounting for this aseismic moment in our calculation of seismic faulting efficiency for the 1993 stimulation, we obtain $\chi = 1.24$ (see Figure 5). This aseismic motion captured by Cornet et al. (1997) is presumably the largest aseismic motion that occurred during the 1993 stimulation. Indeed, it seems unlikely that a larger aseismic motion could have occurred without intersecting the borehole and then be detected. The scenario of $\Delta W_{fault} > \Delta W_H$ indicates that previously stored elastic energy within the reservoir can be released in addition to the energy related to the hydraulic perturbation. In the case of a first injection of fluid into the reservoir, this potentially provides a criterion to determine if seismicity is triggered ($\chi > 1$) or induced ($\chi < 1$). The seismic injection efficiency I_E can also be used as a diagnostic tool to evaluate whether the earthquake is induced or triggered (Goodfellow et al., 2015). However, using this criterion would require setting a threshold to distinguish induced from triggered events, whereas in the formulation with χ , this threshold is naturally equal to 1.

5.2. Difference in Energy Release Between Stimulations and Re-Stimulations

The absence of seismicity at the beginning of a re-stimulation has already been observed and explained as a Kaiser effect (see Section 2.3). This would refer to a memory effect of the initially stimulated volume which only responds seismically when the pressure becomes higher than the maximum pressure reached during the first stimulation. We suggest here that the pre-existing elastic strain energy plays a key role in the seismic response of the reservoir to the injection and this may explain why there is no seismicity at the start of injection and why there is a sharp increase in I_E or χ for an already stimulated reservoir. Like McGarr (2014), we assume that the reservoir is in a critical state before the first stimulation, and that fluid injection perturbs the stimulated volume which controls seismicity. However, we suggest that seismicity is not primarily due to the deformation generated in the

stimulated volume as argued by the model of McGarr (2014), but rather to the release of stored energy. Consequently, during re-stimulation, the reservoir has less pre-existing elastic deformation energy (because it was relaxed by the first stimulation) and requires more loading from the fluid injection to induce seismicity. Once seismicity begins, I_E or χ are initially low, but rapidly increase to a level similar to that of other stimulations. Consequently, the first stimulation would be a “relaxation” stimulation, while the re-stimulation would be a “recharging” stimulation of the reservoir.

5.3. Circulation Episodes

Our results evidence that, for circulation episodes, I_E and χ are on average one order of magnitude smaller than for stimulations and re-stimulations episodes. This difference may arise from several factors. First, we might consider that, as these circulation tests are taking place in previously stimulated reservoirs (similar to re-stimulations) a fraction of the elastic strain energy (conveyed to the reservoir notably by the tectonic stress) available for faulting has already been released. Considering that the circulation tests do not impose significant stress changes outside the already stimulated zone, this could therefore explain the low value of E_R or ΔW_{fault} and therefore the low value of I_E or χ over the whole course of these episodes. We could have expected, given the long duration of circulation tests, that the tectonic loading in terms of elastic strain energy would have become significant during the circulation. This would have led to more energy available for faulting and thus to a higher I_E or χ value than observed. Nonetheless, we can show that the accumulation of this strain energy from tectonic loading is not sufficient during a circulation test. Indeed, maximum strain rate in the Rhine Graben has been estimated to $7 \times 10^{-9} \text{ yr}^{-1}$ (Henron et al., 2020). Considering a 100 days period (typical for a circulation episode), a reservoir volume of 5 km^3 and a representative stress value within the reservoir of 100 MPa (which is the value of the largest principal stress at 4 km depth from Figure 1 and Cornet et al., 2007), we computed an increase of potential strain energy of $1 \times 10^{10} \text{ J}$. This value is small compared to the typical amount of hydraulic energy for a single episode (around 10^{11} J). It suggests that, at the time scale of a single circulation episode, the contribution of the tectonic loading is not sufficient to significantly impact the seismic energy released. The same applies when considering the time between two fluid injection operations, which is around 6 months (Schill et al., 2017). We note, however, that this elastic strain energy accumulates also over long periods without fluid injection and becomes the main reservoir energy driving the seismicity at the time of an injection. This is typically the case for a first stimulation and this confirms our interpretation that the pre-existing strain energy is the main parameter of induced seismicity (see Section 5.2). Thus seismicity during stimulations is more likely to be triggered. On the contrary, during re-stimulations and circulations, it would be largely hydraulic energy that is used for earthquakes which are then more likely to be induced.

Additionally, the low values of I_E or χ could also be due to the potential overestimation of ΔW_H . Indeed, during a circulation test a large amount of fluid is pumped out of the reservoir and reinjected into the reservoir after being cooled through a heat exchanger at the surface. This leads to a reservoir cooling considering the long duration of the test. The fluid is then reinjected into a cooler rock, which in comparison with stimulations, reduces the effects of the thermo-elastic mechanisms behind seismicity. The same reasoning was invoked to explain the low aftershock activity in the Coso geothermal plan following the 2019 Ridgecrest's earthquakes (Im et al., 2021). In this case, the cooling of the reservoir over long time-scale results in less energy available for faulting and an anomalous low seismic activity. However, the thermal effect is not considered in our study, which focuses on comparing the injected energy and the released seismic energy, not on the energy transfers that operate in the reservoir.

Complementing the explanation by reservoir cooling, the difference observed between circulation tests and stimulations could be explained by the fact that there is a certain level of energy dissipation (energy dissipation rate) in the processes that we are not able to observe, and which balances the lower hydraulic energy rate for circulation tests (carried out over a longer period of time than stimulations).

A difference arises when we compare the evolution of I_E or χ during the 2003 and 2010 circulation tests. The evolution of χ during the 2003 circulation episode is characterized by an evolution similar to a stimulation (i.e., almost constant), whereas the 2010 circulation is characterized by a first phase of strong increase of χ , which is similar to a re-stimulation behavior. The quasi-constant evolution during the first phase of the 2003 circulation is probably due to the fact that this injection took place immediately after the 2003 stimulation stopped. Thus, post-injection events may have been accounted for in the circulation whereas they could have been associated with

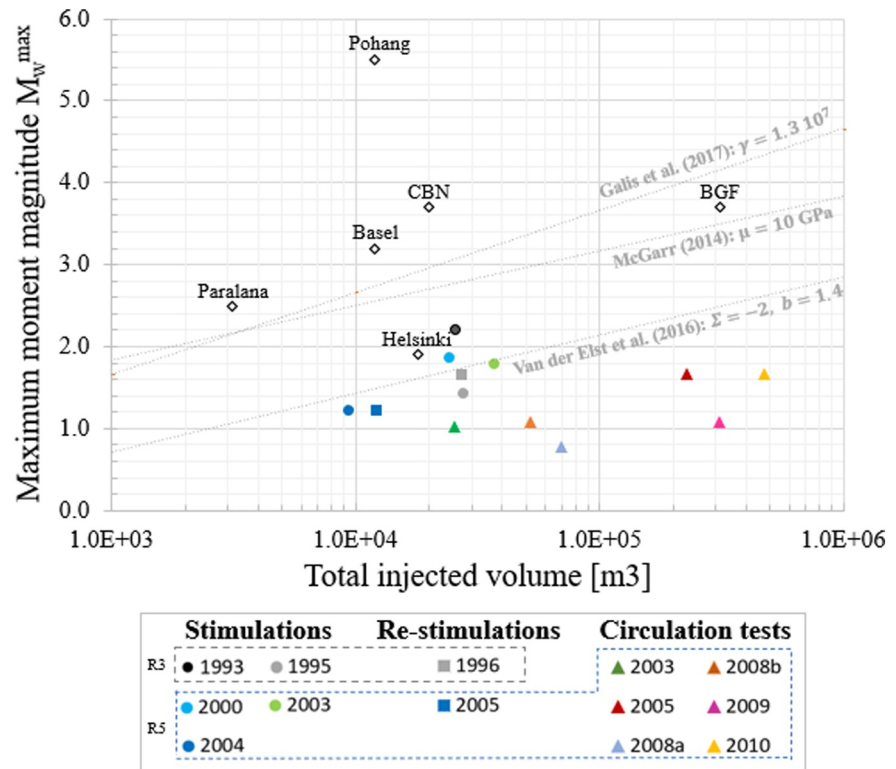


Figure 6. Comparison of the observed maximum magnitude with the total injected volume of each episode of Solfz-sous-Forêts (cf. legend) and for some stimulations carried out in some other Enhanced Geothermal System sites (data from Bentz et al. (2020)). Three models are shown for comparison: McGarr (2014), Van der Elst et al. (2016), and Galis et al. (2017) whose all parameter values are representative of the Solfz-sous-Forêts 1993 stimulation episode (see Section 5.4 for details). (Same color and marker codes as in Figure 3).

stimulation. This explanation is supported by the higher χ and I_E values of the 2003 circulation compared with other circulations.

5.4. Prediction of the Maximum Moment Magnitude

The volume of fluid injected into a reservoir has been used in several cases to estimate the maximum magnitude during injections (Galis et al., 2017; McGarr, 2014; Van der Elst et al., 2016). Our harmonized database allows us to compare in Figure 6, the consistency of the predicted maximum magnitude, \hat{M}_W^{\max} using the three aforementioned models with the observed values, M_W^{\max} in the Solfz-sous-Forêts EGS site. The three models are computed considering a shear modulus of 10 GPa representative of the R3 granite, a seismogenic index of -2 representative of the 1993 stimulation episode (Dinske & Shapiro, 2013) and its computed b-value of 1.4 (see Text S4 in Supporting Information S1). In addition, to compare the Solfz-sous-Forêts observations with other EGS sites, we also represent the observed M_W^{\max} (reported in Bentz et al. (2020)) for six EGS sites around the world: Basel (Switzerland), Cooper Basin (CBN, Australia), Paralana (Australia), Berlin Geothermal Field (BGF, Salvador), Helsinki (Finland) and the near Pohang (South Korea).

We first observe that for similar injected volumes, the models predict \hat{M}_W^{\max} values that can differ by two units. The upper limits of magnitude given by McGarr (2014) and Galis et al. (2017) are well respected. Although the values predicted by the model of Van der Elst et al. (2016) are closer to the observations, they underestimate the observed M_W^{\max} for two stimulations including the 1993 stimulation for which the model is calibrated. When analyzing separately the evolution of the observed M_W^{\max} for the stimulations and the circulation tests, we observe an increase with the total volume injected with a slope well represented by the models. As for the Solfz-sous-Forêts site, all the EGS sites are located in crystalline rock basement with a depth target between 2 km (BGF) and 6 km (Helsinki). We notice that all observed M_W^{\max} in the Solfz-sous-Forêts EGS site are lower than other EGS

sites analyzed. For similar injected volumes, the range of observed M_W^{\max} is large (between 1 and 5.5). This indicates that maximum magnitude is site-dependent and that its prediction should account for the reservoir characteristic properties.

The fact that the values of I_E or χ are almost similar for all stimulations and circulations and during the whole course of the stimulation or circulation leads to consider I_E or χ as a fixed property of the reservoir. It can therefore be used to predict the cumulative seismic moment, $\Sigma\hat{M}_0$ or the maximum moment magnitude, \hat{M}_w^{\max} expected from the hydraulic energy to be injected into the reservoir (from the planned injected volume and the well-head pressure). Performing such a prediction requires an a priori estimate of I_E or χ , possibly from previous stimulations/re-stimulations at the same site. If no such estimate is available from previous injection operations, it is still possible to estimate it during an early stage of an injection. Indeed, as I_E or χ are quasi-constant or are evolving steadily during stimulations, we can get an estimation of them during the beginning of the injection, when the risk of having a large earthquake remains low. This value can then be used to estimate the expected seismic moment for the rest of the injection based on the planned injection. This allows us to predict the expected cumulative seismic moment (or the expected maximum magnitude under assumptions) from the planned hydraulic scenario, $P(V)$ as a function of time. From Equations 14 and 20, one can estimate the expected cumulative seismic moment $\Sigma\hat{M}_0$ based on the hydraulic energy ΔW_H that is planned to be injected knowing an estimate of the seismic injection efficiency:

$$\Sigma\hat{M}_0 = I_E \frac{2\mu}{\Delta\sigma\eta_R} \Delta W_H. \quad (23)$$

Similarly, from an estimate of χ and considering $\sigma_f = \sigma_1$ that is, the upper limit of seismic faulting energy, we have:

$$\Sigma\hat{M}_0 = \chi \frac{2\mu}{\sigma_1 - \sigma_3} \Delta W_H. \quad (24)$$

We then estimate the maximum moment magnitude \hat{M}_w^{\max} from the predicted cumulative seismic moment $\Sigma\hat{M}_0$ similarly to McGarr (2014) and assuming that the Gutenberg-Richter magnitude distribution holds up to the largest magnitudes. Thus, we have

$$\hat{M}_w^{\max} = \frac{2}{3} \log_{10} \left(\frac{3 - 2b}{b} \Sigma\hat{M}_0 \right) - 6.07 \quad (25)$$

where b is the b value.

The approach of Hallo et al. (2014) and Li et al. (2022) is quite similar to ours. Indeed, they also propose predicting the maximum magnitude based on the total seismic moment. The difference lies in how they estimate this seismic moment total. They calculate a theoretical seismic moment from the injected fluid volume (McGarr, 1976), which they then correct using a coefficient, the seismic efficiency ratio (SER, defined as the ratio between the observed cumulative seismic moment and the theoretical cumulative seismic moment). Similarly, the seismogenic index introduced by Shapiro et al. (2010), notably in the model of Van der Elst et al. (2016), is used in a way to adjust the prediction of the maximum magnitude based on the injected volume. While the interpretation of these coefficients (I_E , χ , SER, or seismogenic index) may differ, they all account for the balance between hydraulic energy and released energy.

We illustrate our approach on the 1993 stimulation using χ . We suppose in this example that we have no previous estimate of χ such that we compute this value at several times during the course of the injection. We considered three times after the beginning of the injection: after 5%, 10%, and 15% of the total hydraulic energy. From χ , we then computed the expected cumulative seismic moment at the end of the episode and derived the expected maximum moment magnitude \hat{M}_w^{\max} (Figure 7b). We see that this method provides a reasonable estimation of the $\hat{M}_w^{\max} = 2.05$ (after 15% of hydraulic energy injected) very close to the observed maximum moment magnitude for this stimulation that is, $M_W^{\max} = 2.20$. We apply the same procedure for all stimulations (see Figures S7 to S10 in Supporting Information S1). For re-stimulations, we used the value of χ at the end of the preceding stimulation that took place at the same location in the reservoir (see Figure S11 in Supporting Information S1). We first

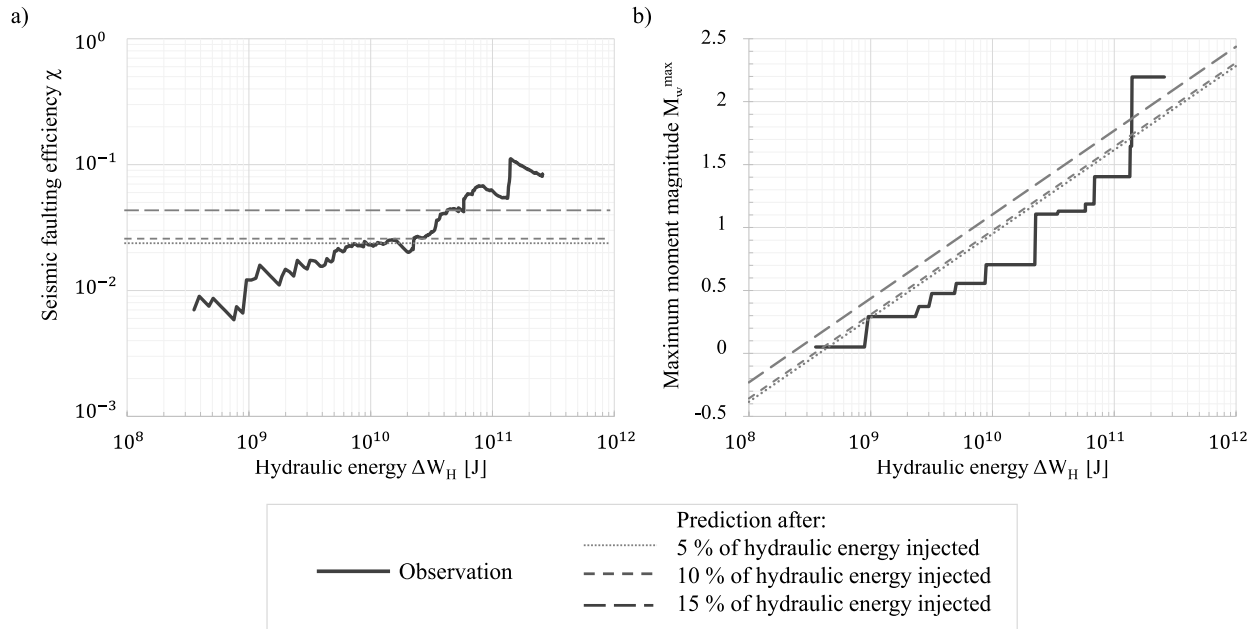


Figure 7. Prediction for the 1993 stimulation episode of (a) the seismic faulting efficiency χ and of (b) the maximum moment magnitude, \hat{M}_w^{\max} from early data (after having injected 5%, 10%, and 15% of the total hydraulic energy).

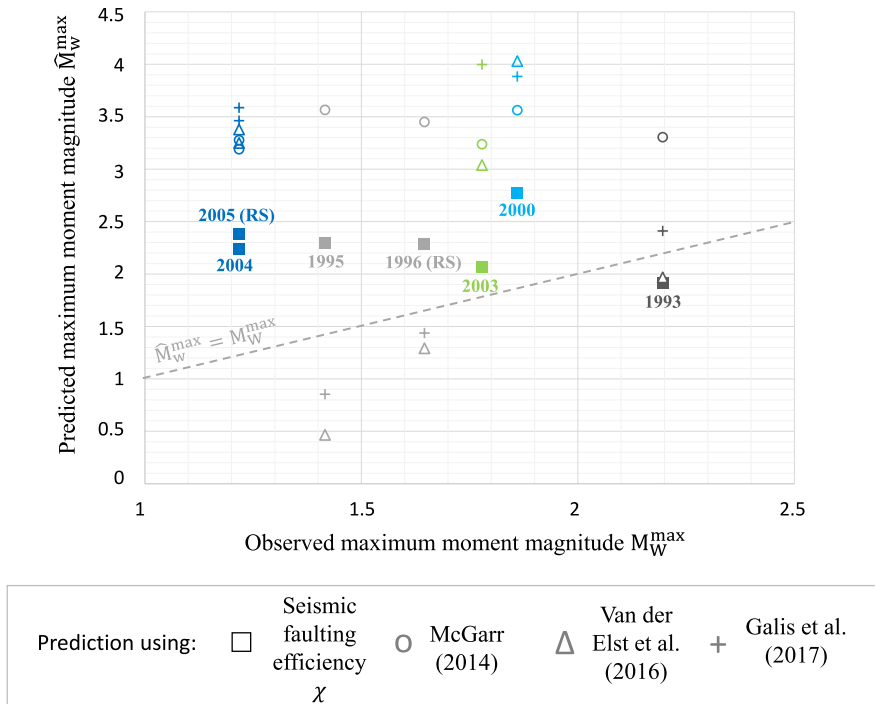


Figure 8. Comparison of the predicted maximum magnitude with observed ones for stimulations based on early data after having injected 10% of hydraulic energy. For re-stimulations, the prediction is made based on the full data of the first associated stimulation. The predicted maximum magnitudes based on three models (Galis et al., 2017; McGarr, 2014; Van der Elst et al., 2016) are represented. The dashed line represents the predicted moment magnitude that would match the observed moment magnitude. (Same color code as in Figure 3).

compared the predicted cumulative seismic moments, $\Sigma\widehat{M}_0$, with the observed ones for each stimulation. We observed an excellent agreement between the two values which suggests that the proposed method is very effective in deriving a predicted seismic moment from the hydraulic data (see Figure S12 in Supporting Information S1). We also obtained the predicted maximum moment magnitude for all stimulation and re-stimulation episodes and compared these values with the observed maximum moment magnitude and the predicted values from three models (Galis et al., 2017; McGarr, 2014; Van der Elst et al., 2016) in Figure 8. The maximum magnitudes predicted using χ (after 10% of hydraulic energy injected) are for almost all episodes close to the observed values with a maximum difference of about one unit. The predictions obtained by the other three models, on the other hand, either overestimate the maximum observed magnitude (with an average difference of two units) or underestimate it. The lowest accuracy of the prediction for \widehat{M}_W^{\max} compared to $\Sigma\widehat{M}_0$ suggests that a difficulty in predicting the largest magnitude resides on the extrapolation of the Gutenberg-Richter magnitude distribution up to larger magnitude events. Indeed, as visible in Figure 3 and already noted by Dorbath et al. (2009), a deficit in large magnitude events is observed such that their number deviates from the expected number interpolating the Gutenberg-Richter distribution obtained from low magnitude events.

As shown in Figure 4 (see Section 4.1), the value of χ at the beginning and end of the injection may not be exactly the same since χ may vary slightly during the injection operation. The prediction can be made more accurate by taking into account these possible slight evolutions of χ . Indeed, instead of using a single value of χ , we can extrapolate the trend of χ during the initial phase of injection to estimate the value of χ at any future time during injection. We thus performed a linear fit between the logarithm of χ and the logarithm of ΔW_H for all stimulations considering the same three times of injection (5%, 10%, and 15% of hydraulic energy injected) and then computed the expected maximum moment magnitude. Figure 7 illustrates this approach for the 1993 stimulation and Figure 8 compares the predicted moment magnitudes with observed ones and the predicted values using the three models (Galis et al., 2017; McGarr, 2014; Van der Elst et al., 2016). We obtained a slightly higher accuracy with this approach, especially for the 1993 stimulation, where we got a maximum moment magnitude $\widehat{M}_W^{\max} = 2.18$ from the data of the first 10% of hydraulic energy injection, matching the observed value closely ($M_W^{\max} = 2.20$).

5.5. Analogy With the Prediction Model of McGarr (2014)

As we shown in the previous section, the linear model of McGarr (2014) is predicting higher maximum magnitude than those using χ by about 1 unit. We here formally compare both models and try to explain the deviation of the maximum magnitude estimates. If we assume that the injected pressure is constant we can notice that hydraulic energy can be simplified as:

$$\Delta W_H \approx P_{in} V \quad (26)$$

where P_{in} is the injection pressure and V is the injected fluid volume. Using Equation 26 in Equation 24, leads to:

$$\Sigma\widehat{M}_0(\chi) \approx \frac{\chi P_{in}}{\sigma_1 - \sigma_3} 2\mu V = \frac{\chi P_{in}}{\sigma_1 - \sigma_3} \Sigma\widehat{M}_0(McGarr) \quad (27)$$

where $\Sigma\widehat{M}_0(\chi)$ and $\Sigma\widehat{M}_0(McGarr)$ are the expected cumulative seismic moment from the use of χ and from the model of McGarr (2014) respectively. Finally, we can estimate the deviation of the expected maximum moment magnitude using χ , $\widehat{M}_W^{\max}(\chi)$ from that using the model of McGarr (2014), $\widehat{M}_W^{\max}(McGarr)$. Indeed, we can notice that:

$$\widehat{M}_W^{\max}(\chi) \approx \widehat{M}_W^{\max}(McGarr) + \frac{2}{3} \log_{10} \left(\frac{\chi P_{in}}{\sigma_1 - \sigma_3} \right). \quad (28)$$

In our case study of Soultz-sous-Forêts, as $\chi < 2.2 \times 10^{-1}$ and $\frac{P_{in}}{\sigma_1 - \sigma_3} < 0.4$, the deviation is estimated to be about -0.8 which is close to the observed deviation.

Although the stimulated volume controls the induced seismicity in both our approach and that of McGarr (2014), the deviation can be explained by the fact that McGarr (2014) considers that the seismicity is mainly induced by

the deformation generated by the injection of fluid into this volume whereas our approach seems to show that it is the relaxation of the pre-existing deformation energy that has been accumulated in this stimulated volume that mainly induces the seismicity (see Section 5.2).

6. Conclusion

Based on the extensive databases of the Soultz-sous-Forêts geothermal site which contains different types of hydraulic tests (stimulation, re-stimulation, and circulation tests) performed at different reservoir depths and with various injection strategies during more than 20 years, we studied the seismic response of the reservoir during fluid injection by analyzing the seismic injection efficiency, I_E and a new introduced parameter, the seismic faulting efficiency, χ . I_E is defined as the ratio between the radiated seismic energy and the hydraulic energy and χ is defined as the ratio between the seismic faulting energy (deformation energy during faulting) and the hydraulic energy. χ accounts for reservoir specific stress conditions and allows aseismic energy release to be quantified if we can estimate the seismic moment associated with aseismic slip. Despite, depending on the availability of stress field data, I_E and χ can be used equivalently, as they appeared to be linearly related if the stress field is homogeneous over the reservoir.

We first compiled and harmonized seismic catalogs to account for differences in network configuration, processing schemes and resulting magnitudes between the sequence of hydraulic tests. In this context, we showed the importance of harmonized data sets (seismic catalogs and production data) for inter-episodes and inter-sites hydro-seismic studies.

We noticed a clear signature of the seismic response characterized by the evolution of I_E or χ values as a function of hydraulic energy, depending on the injection configuration: stimulation, re-stimulation and circulation test. The stimulation and re-stimulation episodes showed similar I_E values (between 1.7×10^{-3} and 5.2×10^{-3}) and χ values (between 4.8×10^{-2} and 2.2×10^{-1}) at the end of the episodes but differ in the evolution during the injection test. While χ is almost constant during the stimulations, we noticed for the re-stimulations very small values of χ before a rapid increase after reaching similar levels of total hydraulic energy injected during the previous stimulation test. Consequently, we interpret this χ evolution as a result of the initially stored elastic strain energy that was released during the first stimulation. This is quite a different interpretation from previous studies, where such a sudden increase in seismic energy with hydraulic energy was interpreted as unstable reservoir behavior.

The circulation tests showed χ values at the end of the episode to be an order of magnitude lower than those of the stimulations and re-stimulations (between 1.5×10^{-3} and 1.1×10^{-2}) which is potentially related to the release of the elastic strain energy initially stored in the reservoir (by tectonic loading) during the preceding stimulations. Similar χ values have been observed for R3 and R5 injection episodes which contrasts with previous studies.

We showed for the 1993 stimulation that χ can be of the order of 1 when taking into account of the aseismic faulting energy (associated with the aseismic slip evidenced). This scenario indicates that previously stored elastic energy within the reservoir can be released in addition to the energy related to the hydraulic perturbation. In the case of a first fluid injection, this potentially provides a criterion to determine if seismicity is triggered ($\chi > 1$) or induced ($\chi < 1$).

Finally, the similar values of I_E or χ for stimulations and re-stimulations lead us to consider these two parameters as a reservoir property describing the seismic response to fluid injection. Based on this, we proposed a method using I_E or χ that has been able to accurately predict the cumulative seismic moment and the largest magnitude of the induced seismic events knowing the maximum targeted hydraulic energy of the injection. Our method is found to be similar to the one proposed by McGarr (2014), but their method tended to overestimate the maximum magnitudes by about 1 unit. Although I_E and χ appear to be linearly linked when the stress field is homogeneous at the reservoir scale and thus both useful for real time monitoring application and seismic hazard assessment, we underline that χ could be especially useful for comparing different reservoirs where high resolution knowledge of the stress field is known.

Data Availability Statement

All hydraulic data and seismological data (waveforms and earthquakes catalogs) of the stimulations and circulation tests used in this study are available in the CDGP (Data Center for Deep Geothermal Energy) at <https://cdgp.u-strasbg.fr>. The homogenized seismological catalogs (with seismic moments and moment magnitudes) and the produced data sets used for the comparison between seismic and hydraulic energy are also available in the CDGP. All these data are grouped by episode and can be accessed using the DOI associated with each episode indicated in the references:

- 1993 stimulation episode: (GEIE-EMC & EOSt, 2019a).
- 1995 stimulation episode: (GEIE-EMC & EOSt, 2019b).
- 1996 stimulation episode: (GEIE-EMC & EOSt, 2019c).
- 2000 stimulation episode: (GEIE-EMC & EOSt, 2018a).
- 2003 stimulation and circulation test episodes: (GEIE-EMC & EOSt, 2018b).
- 2004 stimulation episode: (GEIE-EMC & EOSt, 2018c).
- 2005 stimulation episode: (GEIE-EMC & EOSt, 2018d).
- 2010 circulation test episode: (GEIE-EMC & EOSt, 2019d).

An Authentication, Authorization and Accounting Infrastructure (AAAI) ensures that data distribution respects the intellectual property rights (IPR) of the owner. As such, data can be provided, after registration and entering the user's affiliation (i.e., academic, industrial, ...), either automatically or after approval by the data owner. Some of the data processing is realized with the open source Python program *SourceSpec* (Satriano, 2022).

Acknowledgments

We thank Professors A. McGarr and G. Kwiatek for their helpful comments, which have enabled us to improve the quality of the manuscript. We are also grateful to an anonymous reviewer who carefully checked the manuscript. We thank the GEIE-EMC, the CDGP (Data Center for Deep Geothermal Energy, <https://cdgp.u-strasbg.fr>) and the EPOS TCS-AH platform (European Platform Observing System for Anthropogenic hazards, <https://tcs.ah-epos.eu>) for providing and distributing the data used in this study. This work was performed under the framework of the Laboratory of Excellence LABEX ANR-11-LABX-0050-G-EAU-THERMIE-PROFONDE and the Interdisciplinary Thematic Institute GeoT, as part of the ITI 2021-2028 program of the University of Strasbourg, CNRS and Inserm, supported by IdEx Unistra (ANR 10 IDEX 0002) and by SFRI STRATUS project (ANR 20 SFRI 0012) under the framework of the French Investments for the Future Program.

References

- Abercrombie, R. E. (2021). Resolution and uncertainties in estimates of earthquake stress drop and energy release. *Philosophical Transactions of the Royal Society A*, 379(2196), 20200131. <https://doi.org/10.1098/rsta.2020.0131>
- Aki, K. (1966). Generation and propagation of G waves from the Niigata earthquake of June 16, 1964: Part 2. Estimation of earthquake moment, released energy, and stress-strain drop from the g wave spectrum. *Bulletin of the Earthquake Research Institute, University of Tokyo*, 44(1), 73–88.
- Aki, K., & Richards, P. G. (1980). *Quantitative seismology: Theory and methods* (Vol. 859). Freeman.
- Baisch, S., Vörös, R., Rother, E., Stang, H., Jung, R., & Schellschmidt, R. (2010). A numerical model for fluid injection induced seismicity at Soultz-sous-Forêts. *International Journal of Rock Mechanics and Mining Sciences*, 47(3), 405–413. <https://doi.org/10.1016/j.ijrmm.2009.10.001>
- Baria, R., Jung, R., Tischner, T., Nicholls, J., Michelet, S., Sanjuan, B., et al. (2006). Creation of an HDR reservoir at 5000 m depth at the European HDR project. In *Proceedings, thirty-first workshop on geothermal reservoir engineering*.
- Baria, R., Michelet, S., Baumgärtner, J., Dyer, B., Gerard, A., Nicholls, J., et al. (2004). Microseismic monitoring of the world's largest potential HDR reservoir. In *Proceedings, twenty-ninth workshop on geothermal reservoir engineering*.
- Baujard, C., Schoenball, M., Kohl, T., & Dorbath, L. (2014). Large magnitude events during injections in geothermal reservoirs and hydraulic energy: A heuristic approach. *Geothermics*, 52, 140–152. <https://doi.org/10.1016/j.geothermics.2014.07.002>
- Bentz, S., Kwiatek, G., Martínez-Garzáon, P., Bohnhoff, M., & Dresen, G. (2020). Seismic moment evolution during hydraulic stimulations. *Geophysical Research Letters*, 47(5), e2019GL086185. <https://doi.org/10.1029/2019gl086185>
- Bourouis, S., & Bernard, P. (2007). Evidence for coupled seismic and aseismic fault slip during water injection in the geothermal site of Soultz (France), and implications for seismogenic transients. *Geophysical Journal International*, 169(2), 723–732. <https://doi.org/10.1111/j.1365-246x.2006.03325.x>
- Brune, J. N. (1970). Tectonic stress and the spectra of seismic shear waves from earthquakes. *Journal of Geophysical Research*, 75(26), 4997–5009. <https://doi.org/10.1029/jb075i026p04997>
- Calò, M., & Dorbath, C. (2013). Different behaviours of the seismic velocity field at Soultz-sous-Forêts revealed by 4-D seismic tomography: Case study of GPK3 and GPK2 injection tests. *Geophysical Journal International*, 194(2), 1119–1137. <https://doi.org/10.1093/gji/ggt153>
- Calò, M., Dorbath, C., Cornet, F., & Cuenot, N. (2011). Large-scale aseismic motion identified through 4-DP-wave tomography. *Geophysical Journal International*, 186(3), 1295–1314. <https://doi.org/10.1111/j.1365-246x.2011.05108.x>
- Cauchie, L., Lengliné, O., & Schmittbuhl, J. (2020). Seismic asperity size evolution during fluid injection: Case study of the 1993 Soultz-sous-Forêts injection. *Geophysical Journal International*, 221(2), 968–980. <https://doi.org/10.1093/gji/ggaa051>
- Charléty, J., Cuenot, N., Dorbath, L., Dorbath, C., Haessler, H., & Frogneux, M. (2007). Large earthquakes during hydraulic stimulations at the geothermal site of Soultz-sous-Forêts. *International Journal of Rock Mechanics and Mining Sciences*, 44(8), 1091–1105. <https://doi.org/10.1016/j.ijrmm.2007.06.003>
- Cornet, F. H. (2016). Seismic and aseismic motions generated by fluid injections. *Geomechanics for Energy and the Environment*, 5, 42–54. <https://doi.org/10.1016/j.gete.2015.12.003>
- Cornet, F. H., Bérard, T., & Bourouis, S. (2007). How close to failure is a granite rock mass at a 5 km depth? *International Journal of Rock Mechanics and Mining Sciences*, 44(1), 47–66. <https://doi.org/10.1016/j.ijrmm.2006.04.008>
- Cornet, F. H., Helm, J., Poitrenaud, H., & Etchecopar, A. (1997). Seismic and aseismic slips induced by large-scale fluid injections. In *Seismicity associated with mines, reservoirs and fluid injections* (pp. 563–583). Springer.
- Cuenot, N., Charléty, J., Dorbath, L., & Haessler, H. (2006). Faulting mechanisms and stress regime at the European HDR site of Soultz-sous-Forêts, France. *Geothermics*, 35(5–6), 561–575. <https://doi.org/10.1016/j.geothermics.2006.11.007>

- Cuenot, N., Dorbath, C., & Dorbath, L. (2008). Analysis of the microseismicity induced by fluid injections at the EGS site of Soultz-sous-Forêts (Alsace, France): Implications for the characterization of the geothermal reservoir properties. *Pure and Applied Geophysics*, *165*(5), 797–828. <https://doi.org/10.1007/s00024-008-0335-7>
- Cuenot, N., Frogneux, M., Dorbath, C., & Calo, M. (2011). Induced microseismic activity during circulation tests at the EGS site of Soultz-sous-Forêts (France). In *Thirty-sixth workshop on geothermal reservoir engineering, Stanford, California*.
- De Barros, L., Cappa, F., Guglielmi, Y., Duboeuf, L., & Grasso, J.-R. (2019). Energy of injection-induced seismicity predicted from in-situ experiments. *Scientific Reports*, *9*(1), 1–11. <https://doi.org/10.1038/s41598-019-41306-x>
- Dezayes, C., Genter, A., & Hooijkaas, G. R. (2005). Deep-seated geology and fracture system of the EGS Soultz reservoir (France) based on recent 5 km depth boreholes. In *Proceedings world geothermal congress* (pp. 24–29).
- Dezayes, C., Genter, A., & Valley, B. (2010). Structure of the low permeable naturally fractured geothermal reservoir at Soultz. *Comptes Rendus Geoscience*, *342*(7), 517–530. <https://doi.org/10.1016/j.crte.2009.10.002>
- Dinske, C., & Shapiro, S. A. (2013). Seismotectonic state of reservoirs inferred from magnitude distributions of fluid-induced seismicity. *Journal of Seismology*, *17*(1), 13–25. <https://doi.org/10.1007/s10950-012-9292-9>
- Dorbath, L., Cuenot, N., Genter, A., & Frogneux, M. (2009). Seismic response of the fractured and faulted granite of Soultz-sous-Forêts (France) to 5 km deep massive water injections. *Geophysical Journal International*, *177*(2), 653–675. <https://doi.org/10.1111/j.1365-246x.2009.04030.x>
- Douglas, J., Edwards, B., Convertito, V., Sharma, N., Tramelli, A., Kraaijpoel, D., et al. (2013). Predicting ground motion from induced earthquakes in geothermal areas. *Bulletin of the Seismological Society of America*, *103*(3), 1875–1897. <https://doi.org/10.1785/0120120197>
- Ellsworth, W. L. (2013). Injection-induced earthquakes. *Science*, *341*(6142), 1225942. <https://doi.org/10.1126/science.1225942>
- Evans, K. F., Zappone, A., Kraft, T., Deichmann, N., & Moia, F. (2012). A survey of the induced seismic responses to fluid injection in geothermal and CO₂ reservoirs in Europe. *Geothermics*, *41*, 30–54. <https://doi.org/10.1016/j.geothermics.2011.08.002>
- Galis, M., Ampuero, J. P., Mai, P. M., & Cappa, F. (2017). Induced seismicity provides insight into why earthquake ruptures stop. *Science Advances*, *3*(12), eaap7528. <https://doi.org/10.1126/sciadv.aap7528>
- Gaucher, E., & Kohl, T. (2014). Are the seismogenic responses of the Soultz and the Großschönebeck enhanced geothermal fields understood. In *74th annual meeting of the German geophysical society (DGG)*.
- Gaucher, E., Schoenball, M., Heidbach, O., Zang, A., Fokker, P. A., van Wees, J.-D., & Kohl, T. (2015). Induced seismicity in geothermal reservoirs: A review of forecasting approaches. *Renewable and Sustainable Energy Reviews*, *52*, 1473–1490. <https://doi.org/10.1016/j.rser.2015.08.026>
- GEIE-EMCEOST. (2018a). Episode: 2000 stimulation Soultz-sous-Forêts [Dataset]. *EOST*. <https://doi.org/10.25577/SSFS2000>
- GEIE-EMCEOST. (2018b). Episode: 2003 stimulation Soultz-sous-Forêts [Dataset]. *EOST*. <https://doi.org/10.25577/SSFS2003>
- GEIE-EMCEOST. (2018c). Episode: 2004 stimulation Soultz-sous-Forêts [Dataset]. *EOST*. <https://doi.org/10.25577/SSFS2004>
- GEIE-EMCEOST. (2018d). Episode: 2005 stimulation Soultz-sous-Forêts [Dataset]. *EOST*. <https://doi.org/10.25577/SSFS2005>
- GEIE-EMCEOST. (2019a). Episode: 1993 stimulation and hydraulic tests Soultz-sous-Forêts [Dataset]. *EOST*. <https://doi.org/10.25577/SSFS1993>
- GEIE-EMCEOST. (2019b). Episode: 1995 stimulation and hydraulic tests Soultz-sous-Forêts [Dataset]. *EOST*. <https://doi.org/10.25577/SSFS1995>
- GEIE-EMCEOST. (2019c). Episode: 1996 stimulation and hydraulic tests Soultz-sous-Forêts [Dataset]. *EOST*. <https://doi.org/10.25577/SSFS1996>
- GEIE-EMCEOST. (2019d). Episode: 2010 circulation Soultz-sous-Forêts [Dataset]. *EOST*. <https://doi.org/10.25577/SSFC2010>
- Genter, A., Goerke, X., Graff, J.-J., Cuenot, N., Krall, G., Schindler, M., & Ravier, G. (2010). Current status of the EGS Soultz geothermal project (France). In *World geothermal congress, WGC2010, Bali, Indonesia* (pp. 25–29).
- Gérard, A., Menjöz, A., & Schwoerer, P. (1984). L'anomalie thermique de Soultz-sous-Forêts. *Géotherm Actual*, *3*, 35–42.
- Giardini, D. (2009). Geothermal quake risks must be faced. *Nature*, *462*(7275), 848–849. <https://doi.org/10.1038/462848a>
- Goodfellow, S., Nasser, M., Maxwell, S., & Young, R. (2015). Hydraulic fracture energy budget: Insights from the laboratory. *Geophysical Research Letters*, *42*(9), 3179–3187. <https://doi.org/10.1002/2015gl063093>
- Grigoli, F., Cesca, S., Rinaldi, A. P., Manconi, A., Lopez-Comino, J. A., Clinton, J., et al. (2018). The November 2017 Mw 5.5 Pohang earthquake: A possible case of induced seismicity in South Korea. *Science*, *360*(6392), 1003–1006. <https://doi.org/10.1126/science.aat2010>
- Gutenberg, B., & Richter, C. F. (1944). Frequency of earthquakes in California. *Bulletin of the Seismological Society of America*, *34*(4), 185–188. <https://doi.org/10.1785/bssa0340040185>
- Gutenberg, B., & Richter, C. F. (1956). Magnitude and energy of earthquakes. *Annals of Geophysics*, *9*(1), 1–15.
- Hallo, M., Oprsal, I., Eisner, L., & Ali, M. Y. (2014). Prediction of magnitude of the largest potentially induced seismic event. *Journal of Seismology*, *18*(3), 421–431. <https://doi.org/10.1007/s10950-014-9417-4>
- Hanks, T. C., & Kanamori, H. (1979). A moment magnitude scale. *Journal of Geophysical Research*, *84*(B5), 2348–2350. <https://doi.org/10.1029/jb084ib05p02348>
- Henrion, E., Masson, F., Doubré, C., Ulrich, P., & Meghraoui, M. (2020). Present-day deformation in the Upper Rhine Graben from GNSS data. *Geophysical Journal International*, *223*(1), 599–611. <https://doi.org/10.1093/gji/ggaa320>
- Husseini, M. I., & Randall, M. (1976). Rupture velocity and radiation efficiency. *Bulletin of the Seismological Society of America*, *66*(4), 1173–1187.
- Ide, S., & Beroza, G. C. (2001). Does apparent stress vary with earthquake size? *Geophysical Research Letters*, *28*(17), 3349–3352. <https://doi.org/10.1029/2001gl013106>
- Im, K., Avouac, J.-P., Heimisson, E. R., & Elsworth, D. (2021). Ridgecrest aftershocks at Coso suppressed by thermal distressing. *Nature*, *595*(7865), 70–74. <https://doi.org/10.1038/s41586-021-03601-4>
- Jaeger, J. C., Cook, N. G., & Zimmerman, R. (2009). *Fundamentals of rock mechanics*. John Wiley & Sons.
- Jones, R. H. (1997). Source parameters calculations for 1993, 1994, 1995 and 1996 Soultz microseismic data. Socomine report.
- Jupe, A., Jones, R., Willis-Richards, J., Dyer, B., Nicholls, J., & Jacques, P. (1994). *Report on HDR phase 4—Soultz experimental programme 1993/1994, IR02/12*. CSM Associates Ltd.
- Kanamori, H., & Brodsky, E. E. (2004). The physics of earthquakes. *Reports on Progress in Physics*, *67*(8), 1429–1496. <https://doi.org/10.1088/0034-4885/67/8/r03>
- Kanamori, H., Mori, J., Hauksson, E., Heaton, T. H., Hutton, L. K., & Jones, L. M. (1993). Determination of earthquake energy release and M_L using terrascopes. *Bulletin of the Seismological Society of America*, *83*(2), 330–346.
- Kanamori, H., Teisseyre, R., & Majewski, E. (2001). Energy budget of earthquakes and seismic efficiency. *Earthquake Thermodynamics and Phase Transformations in the Earth's Interior*, *76*, 293–305. [https://doi.org/10.1016/s0074-6142\(01\)80087-5](https://doi.org/10.1016/s0074-6142(01)80087-5)

- Knopoff, L. (1958). Energy release in earthquakes. *Geophysical Journal International*, 1(1), 44–52. <https://doi.org/10.1111/j.1365-246x.1958.tb00033.x>
- Kostrov, V. (1974). Seismic moment and energy of earthquakes, and seismic flow of rock. *Izvestiya, Academy of Sciences USSR Physics Solid Earth, English Translation*, 1, 23–44.
- Kwiatek, G., Martínez-Garzón, P., Plenkers, K., Leonhardt, M., Zang, A., Von Specht, S., et al. (2018). Insights into complex subdecimeter fracturing processes occurring during a water injection experiment at depth in Åspö Hard Rock Laboratory, Sweden. *Journal of Geophysical Research: Solid Earth*, 123(8), 6616–6635. <https://doi.org/10.1029/2017jb014715>
- Kwiatek, G., Saarno, T., Ader, T., Bluemle, F., Bohnhoff, M., Chendorain, M., et al. (2019). Controlling fluid-induced seismicity during a 6.1-km-deep geothermal stimulation in Finland. *Science Advances*, 5(5), eaav7224. <https://doi.org/10.1126/sciadv.aav7224>
- Lee, K.-K., Ellsworth, W. L., Giardini, D., Townend, J., Ge, S., Shimamoto, T., et al. (2019). Managing injection-induced seismic risks. *Science*, 364(6442), 730–732. <https://doi.org/10.1126/science.aax1878>
- Lengliné, O., Boubacar, M., & Schmittbuhl, J. (2017). Seismicity related to the hydraulic stimulation of GRT1, Rittershoffen, France. *Geophysical Journal International*, 208(3), 1704–1715.
- Li, Z., Eaton, D., & Davidsen, J. (2022). Short-term forecasting of M_{max} during hydraulic fracturing. *Scientific Reports*, 12(1), 12509. <https://doi.org/10.1038/s41598-022-15365-6>
- Madariaga, R. (1976). Dynamics of an expanding circular fault. *Bulletin of the Seismological Society of America*, 66(3), 639–666. <https://doi.org/10.1785/bssa0660030639>
- Majer, E. L., Baria, R., Stark, M., Oates, S., Bommer, J., Smith, B., & Asanuma, H. (2007). Induced seismicity associated with enhanced geothermal systems. *Geothermics*, 36(3), 185–222. <https://doi.org/10.1016/j.geothermics.2007.03.003>
- McGarr, A. (1976). Seismic moments and volume changes. *Journal of Geophysical Research*, 81(8), 1487–1494. <https://doi.org/10.1029/jb081i008p01487>
- McGarr, A. (1999). On relating apparent stress to the stress causing earthquake fault slip. *Journal of Geophysical Research*, 104(B2), 3003–3011. <https://doi.org/10.1029/1998jb900083>
- McGarr, A. (2014). Maximum magnitude earthquakes induced by fluid injection. *Journal of Geophysical Research: Solid Earth*, 119(2), 1008–1019. <https://doi.org/10.1002/2013jb010597>
- McGarr, A., & Barbour, A. J. (2018). Injection-induced moment release can also be aseismic. *Geophysical Research Letters*, 45(11), 5344–5351. <https://doi.org/10.1029/2018gl078422>
- Meixner, J., Schill, E., Grimmer, J. C., Gaucher, E., Kohl, T., & Klingler, P. (2016). Structural control of geothermal reservoirs in extensional tectonic settings: An example from the upper Rhine Graben. *Journal of Structural Geology*, 82, 1–15. <https://doi.org/10.1016/j.jsg.2015.11.003>
- Mukuhira, Y., Dinske, C., Asanuma, H., Ito, T., & Häring, M. (2017). Pore pressure behavior at the shut-in phase and causality of large induced seismicity at Basel, Switzerland. *Journal of Geophysical Research: Solid Earth*, 122(1), 411–435. <https://doi.org/10.1002/2016jb013338>
- Pearson, C. (1981). The relationship between microseismicity and high pore pressures during hydraulic stimulation experiments in low permeability granitic rocks. *Journal of Geophysical Research*, 86(B9), 7855–7864. <https://doi.org/10.1029/jb086ib09p07855>
- Randall, M. J. (1972). Stress drop and the ratio of seismic energy to moment. *Journal of Geophysical Research*, 77(5), 969–970. <https://doi.org/10.1029/jb077i005p00969>
- Satriano, C. (2022). Sourcespec—Earthquake source parameters from p- or s-wave displacement spectra [Software]. *Zenodo*. <https://doi.org/10.5281/ZENODO.3688587>
- Sausse, J., Dezayes, C., Dorbath, L., Genter, A., & Place, J. (2010). 3D model of fracture zones at Soultz-sous-Forêts based on geological data, image logs, induced microseismicity and vertical seismic profiles. *Comptes Rendus Geoscience*, 342(7–8), 531–545. <https://doi.org/10.1016/j.crte.2010.01.011>
- Schill, E., Genter, A., Cuenot, N., & Kohl, T. (2017). Hydraulic performance history at the Soultz EGS reservoirs from stimulation and long-term circulation tests. *Geothermics*, 70, 110–124. <https://doi.org/10.1016/j.geothermics.2017.06.003>
- Shapiro, S. A., Dinske, C., Langenbruch, C., & Wenzel, F. (2010). Seismogenic index and magnitude probability of earthquakes induced during reservoir fluid stimulations. *The Leading Edge*, 29(3), 304–309. <https://doi.org/10.1190/1.3353727>
- Shearer, P. M. (2019). *Introduction to seismology*. Cambridge University Press.
- Udias, A., Vallina, A. U., Madariaga, R., & Buforn, E. (2014). *Source mechanisms of earthquakes: Theory and practice*. Cambridge University Press.
- Vallier, B., Magnenet, V., Schmittbuhl, J., & Fond, C. (2019). Large scale hydro-thermal circulation in the deep geothermal reservoir of Soultz-sous-Forêts (France). *Geothermics*, 78, 154–169. <https://doi.org/10.1016/j.geothermics.2018.12.002>
- Van der Elst, N. J., Page, M. T., Weiser, D. A., Goebel, T. H. W., & Hossein, S. M. (2016). Induced earthquake magnitudes are as large as (statistically) expected. *Journal of Geophysical Research: Solid Earth*, 121(6), 4575–4590. <https://doi.org/10.1002/2016jb012818>
- Vidal, J., Genter, A., & Schmittbuhl, J. (2015). How do permeable fractures in the Triassic sediments of northern Alsace characterize the top of hydrothermal convective cells? Evidence from Soultz geothermal boreholes (France). *Geothermal Energy*, 3(1), 1–28. <https://doi.org/10.1186/s40517-015-0026-4>
- Wiemer, S., & Wyss, M. (2000). Minimum magnitude of completeness in earthquake catalogs: Examples from Alaska, the Western United States, and Japan. *Bulletin of the Seismological Society of America*, 90(4), 859–869. <https://doi.org/10.1785/0119990114>
- Wüstenhagen, R., Wolsink, M., & Bürer, M. J. (2007). Social acceptance of renewable energy innovation: An introduction to the concept. *Energy Policy*, 35(5), 2683–2691. <https://doi.org/10.1016/j.enpol.2006.12.001>
- Zang, A., Oye, V., Jousset, P., Deichmann, N., Gritto, R., McGarr, A., et al. (2014). Analysis of induced seismicity in geothermal reservoirs—An overview. *Geothermics*, 52, 6–21. <https://doi.org/10.1016/j.geothermics.2014.06.005>

References From the Supporting Information

- Aki, K. (1965). Maximum likelihood estimate of b in the formula $\log N = a - bM$ and its confidence limits. *Bull. Earthq. Res. Inst., Tokyo Univ.*, 43, 237–239.
- Baria, R., Baumgartner, J., & Gérard, A. (1996). European hot dry rock programme 1992–1995. In *Extended summary of the final report to EC (DGXII). Contract JOU2-CT92-0115*.
- Baria, R., Baumgartner, J., Gérard, A., Jung, R., & Garnish, J. (1999). European HDR research programme at Soultz-sous-Forêts (France) 1987–1996. *Geothermics*, 28(4), 655–669. [https://doi.org/10.1016/S0375-6505\(99\)00036-X](https://doi.org/10.1016/S0375-6505(99)00036-X)
- Baumgartner, J., Moore, P., & Gérard, A. (2007). Drilling of hot and fractured granite at Soultz-sous-Forêts. In *Engine mid-term conference* (pp. 9–12).

- Baumgärtner, J., Jung, R., Gérard, A., Baria, R., & Garnish, J. (1996). The European HDR project at Soultz-sous-Forêts: Stimulation of the second deep well and first circulation experiments. In *Proceedings of the 21st workshop on geothermal reservoir engineering*. Stanford University.
- Brown, G. O. (2003). The history of the Darcy-Weisbach equation for pipe flow resistance. In *Environmental and water resources history* (pp. 34–43).
- Cao, A., & Gao, S. S. (2002). Temporal variation of seismic b-values beneath northeastern Japan island arc. *Geophysical Research Letters*, 29(9), 48-1–48-3. <https://doi.org/10.1029/2001GL013775>
- Dezayes, C., Genter, A., & Gentier, S. (2005). *Deep geothermal energy in Western Europe: The Soultz project-final report (open file no. BRGM/RP-54227-fr)*. BRGM.
- Reynolds, O. (1883). XXIX. An experimental investigation of the circumstances which determine whether the motion of water shall be direct or sinuous, and of the law of resistance in parallel channels. *Philosophical Transactions of the Royal society of London*, 174, 935–982.
- Tischner, T., Schindler, M., Jung, R., & Nami, P. (2007). HDR project Soultz: Hydraulic and seismic observations during stimulation of the 3 deep wells by massive water injections. In *Proceedings, 32nd workshop on geothermal engineering, Stanford university, Stanford, California* (pp. 22–24).